Electronic Supplementary Information (ESI)

Supplementary Information

Biomimetic Salt-Excreting 2D Evaporator Enables Spatially Decoupled Evaporation, Salt Harvesting, and Energy Recovery for Sustainable Brine Treatment

Haifeng Zhou[1,2], Li Han[3], Chengkai Mao[4], Jiali Jiang[1,2], Hongjuan Ma[3], Long Zhao[1]*
[1] State Key Laboratory of Advanced Electromagnetic Technology, School of Electrical and Electronic Engineering, Huazhong University of Science and Technology, Wuhan 430074, China.

[2] School of Chemistry and Chemical Engineering, Huazhong University of Science and Technology, Wuhan 430074, China.

[3] Shanghai Applied Radiation Institute, School of Environmental and Chemical Engineering, Shanghai University, Shanghai, 200444, China.

[4] College of Chemical Engineering, Fuzhou University, 350116, Fuzhou, China.
*Corresponding author Email: zhaolong@hust.edu.cn

Table of Content:
Section 1:
Theoretical analysis
Section 2:
Supplementary Figures: Fig. S1-S55
Section 3:
Supplementary Table: Table S1-S5

Section 1.

Theoretical analysis of Marangoni effect

The Marangoni effect refers to the mass transfer occurring at the interface between two fluids due to variations in surface tension. Surface tension can be influenced by temperature and solute concentration, as outlined in the following equation:

1. Porous Media Mass Transfer Module:

The governing equations for mass transfer in porous media are implemented.

The mass balance equation is given by:

$$\varepsilon \frac{\partial c}{\partial t} + \nabla \cdot \mathbf{J} = R$$

Where c is the salt concentration, J is the mass flux vector, ε is the porosity (ε=0.9), and R is the reaction source term (R=0).

The mass flux J is defined by:

$$\mathbf{J} = -D_e \nabla c$$

Where D_e is the effective mass transfer coefficient of the fluid within the porous media (10^{-8} m^2/s). The porous media mass transfer follows the Millington-Quirk model:

$$D_e = \frac{\varepsilon}{\varepsilon^{-\frac{1}{3}}} D_c$$

Where D_c is the intrinsic diffusion coefficient of the fluid.

The saturated concentration within the porous media for this model is defined as:

$$c_{\max} = \frac{\rho_w}{M_w} \cdot \varepsilon$$

Where $c_{\max}$ is the saturated concentration of salt within the media, ρ_w is the density of water, and M_w is the molar mass of water.

The boundary condition at the interface with water is set to the saturated concentration. The boundary exposed to air is set as a water evaporation flux boundary. This evaporation flux is positively correlated with temperature and negatively correlated with water content.

Heat Transfer Module:

The governing equations for heat transfer are implemented. The energy balance equation is given by:

$$\rho C_p \frac{\partial T}{\partial t} + \rho C_p \mathbf{u} \cdot \nabla T + \nabla \cdot \mathbf{q} = Q$$

$$\mathbf{q} = -k \nabla T$$

Where ρ is the material density, C_p is the material's specific heat capacity, u is the spatial fluid velocity field vector, T is temperature, q is the heat flux vector, and Q is the heat source power.

The equivalent material parameters are defined by volume averaging as follows:

$$k_{eq} = k_s \cdot V_s\% + k_w \cdot V_w\% + k_a \cdot V_a\%$$

$$\rho_{eq} = \rho_s \cdot V_s\% + \rho_w \cdot V_w\% + \rho_a \cdot V_a\%$$

$$C_{eq} = C_s \cdot V_s\% + C_w \cdot V_w\% + C_a \cdot V_a\%$$

Where k is the thermal conductivity of the material.

In this project, the initial fluid velocity is set to 0. External heat sources include radiation from light illumination and the latent heat of evaporation. The latent heat of evaporation is a function of temperature, exhibiting a negative correlation. The external light source is solar radiation. Accounting for surface roughness and calibrated against experimental temperature measurements, the power is approximately 1000 W/m². Furthermore, as the thermal conductivity of the material varies with water content, an average equivalent method is used to calculate the local thermal conductivity, local density, and local specific heat capacity of the material.

3. Laminar Flow Module PDEs:

The governing equations for laminar flow are implemented. The momentum balance equation is given by:

$$\rho \frac{\partial \mathbf{u}}{\partial t} + \rho(\mathbf{u} \cdot \nabla)\mathbf{u} = \nabla \cdot \left[-p\mathbf{I} + \mu\left(\nabla \mathbf{u} + (\nabla \mathbf{u})^T\right)\right] + \mathbf{F} + \rho \mathbf{g}$$

Where ρ is the fluid density, u is the fluid velocity field vector, p is pressure, I is the identity tensor, F is the applied volume force vector, and μ is the dynamic viscosity (1.8 mPa·s).

The mass balance (continuity) equation is given by:

$$\rho \nabla \cdot \mathbf{u} = 0$$

4. Marangoni Effect:

The Marangoni effect, describing flow driven by surface tension gradients, is incorporated.

The boundary condition related to surface tension gradients is applied:

$$\mathbf{n} \cdot \left[-p\mathbf{I} + \mu\left(\nabla \mathbf{u} + (\nabla \mathbf{u})^T\right)\right] = \delta(\nabla \cdot \mathbf{n})\mathbf{n} - \nabla \delta$$

(Where δ is surface tension, n is the normal unit vector, τ is the tangential direction)

The surface tension coefficient equation is expressed as:

$$\begin{aligned} \delta = {} & T^2 \times 2.3519705 \times 10^{-7} [N/m/K\verb|^|2] - T \times 1.63350014 \times 10^{-5} [N/m/K] \\ & + 0.0977001279 [N/m] + c_{NaCl} \times 1.65027 \times 10^{-6} [N/m] \end{aligned}$$

(Typically a function of concentration and/or temperature)

The specific functional form of δ would depend on the fluid properties being modeled

Section 2. Fig.s

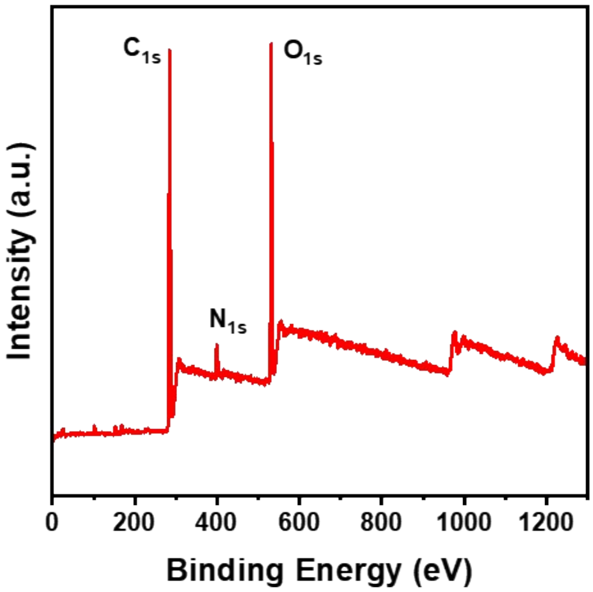

Fig. S1. XPS spectra of PVIL hydrogel.

As shown in **Fig. S1**, XPS testing results indicate elemental contents of 69.98% carbon, 23.64% oxygen, 6.06% nitrogen, and 0.32% bromine, confirming the successful polymerization and cross-linking of VEIMBr.

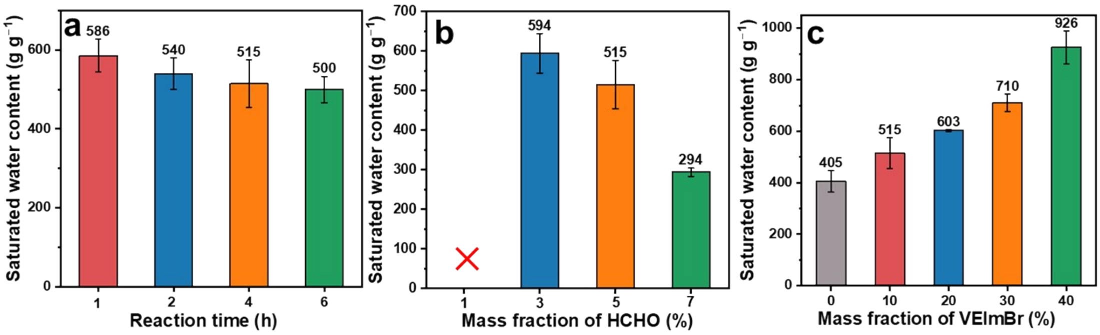

Fig. S2 Water absorption capability of PVIL hydrogel, (a) different reaction time, (b) different HCHO content, (c) different [VEIM]Br content.

The saturated water absorption capacity of PVIL hydrogels prepared under different conditions was also systematically investigated. As shown in **Fig. S2a**, the saturated water absorption capacity decreased with increasing reaction time. This was attributed to increased crosslinking density, which resulted in the formation of more hydrophobic regions. Water absorption capacity decreases from 594% to 294% as formaldehyde content increases from 3% to 7%, due to reduced free volume resulting from higher cross-linking density (**Fig. S2b**). Conversely, absorption increases with [VEIM]Br content, reaching 916% at 40%, highlighting its critical role in enhancing hydrophilicity (**Fig. S2c**). It is worth noting that the trend shown by the saturated water absorption capacity is similar to that of tensile strength, both of which are caused by changes in pores due to an increase in internal cross-linking density. This suggests that it is necessary to select an appropriate pore size to balance strength and water absorption capacity.

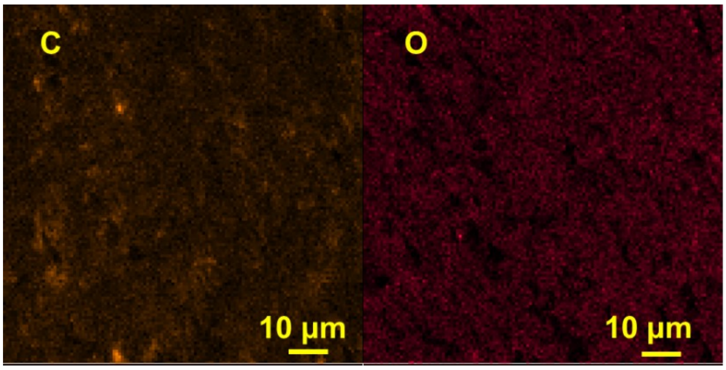

Fig. S3. EDS mapping image of P hydrogel.

EDS imaging confirms the uniform distribution of C and O elements within the P hydrogel.

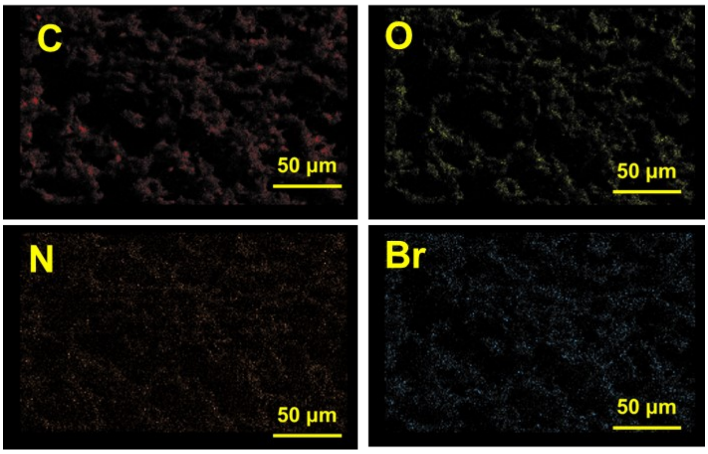

Fig. S4. EDS mapping image of PVIL hydrogel.

EDS imaging confirms the uniform distribution of C, O, N and Br elements within the PVIL hydrogel.

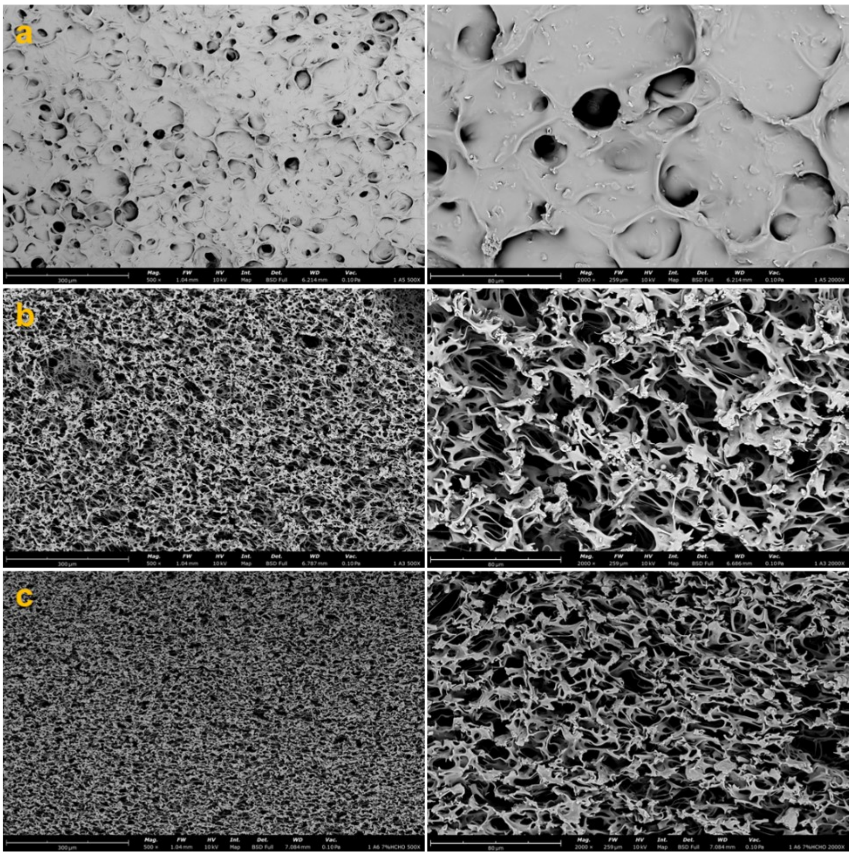

Fig. S5. SEM image of PVIL hydrogel with different formaldehyde (HCHO)content, (a) 3% HCHO, (b) 5% HCHO, (c) 7% HCHO. The image on the right is the corresponding magnification of the image on the left.

Fig. S5 displays SEM images of PVIL hydrogels with different concentrations of HCHO as the cross-linking agent. It can be observed that as the HCHO content increases, the internal pore size of the PVIL hydrogels progressively diminishes, a phenomenon attributable to the heightened cross-linking density.

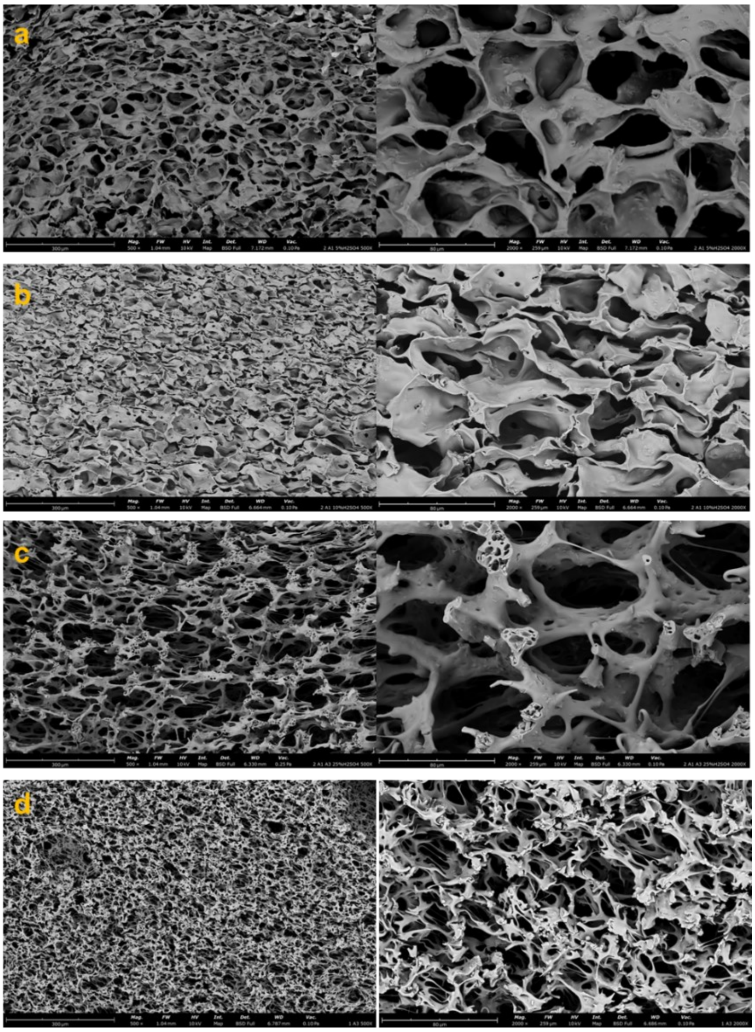

Fig. S6. SEM image of PVIL hydrogel with different H_2SO_4 content, (a) 5%, (b) 10%, (c) 25%, (d) 50%. The image on the right is the corresponding magnification of the image on the left.

Add H_2SO_4 of varying mass fractions to the solution, maintaining a consistent quantity added. The increase in pore size with decreasing sulfuric acid concentration is directly linked to its role as a catalyst in forming the first PVA network. A higher acid concentration catalyzes a faster and more efficient acetal crosslinking reaction, leading to a denser initial PVA network with a smaller mesh size. This constrained structure templates the formation of the subsequent PVIL network under electron-beam irradiation, resulting in a final hydrogel with smaller pores. Conversely, a lower acid concentration results in a slower reaction and a less crosslinked, more open initial PVA network. This provides greater space for the second network to form, ultimately yielding a hydrogel with a larger average pore size. Thus, acid concentration effectively tunes the microstructure by controlling the crosslinking density of the foundational network.

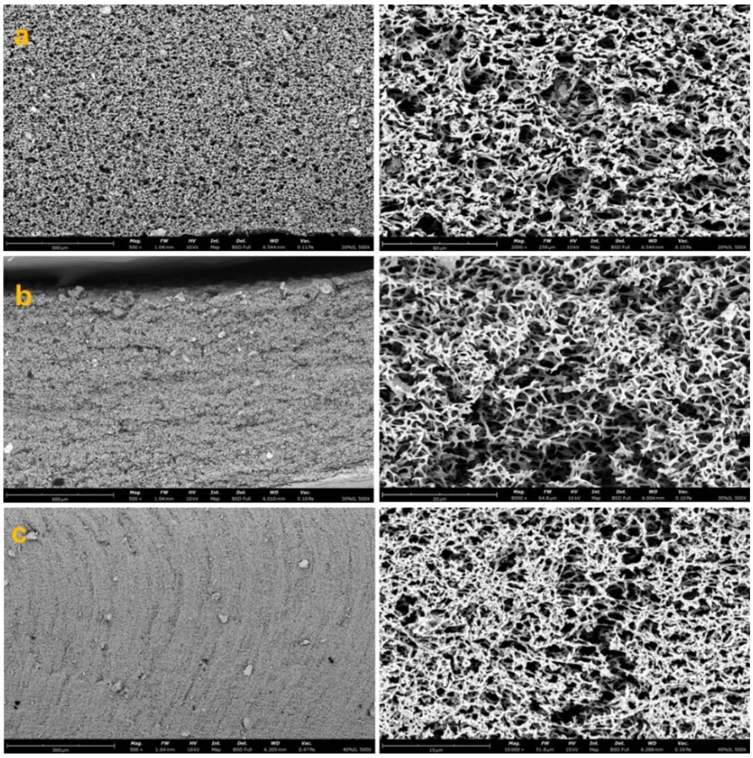

Fig. S7. SEM image of PVIL hydrogel with different IL content, (a) 20%, (b) 30%, (c) 40%. The image on the right is the corresponding magnification of the image on the left.

As shown in **Fig. S7**, from 10% to 40% IL, pore size decreases and densifies. At high concentrations, the IL's role shifts to an active crosslinker. Its polymerization creates a dense second network, and the strong electrostatic/hydrogen bonding interactions between the PVA and PVIL networks significantly increase the overall crosslinking density, producing smaller and more numerous pores. In short, the transition is from a dilution effect (dominating at low IL) to a crosslinking

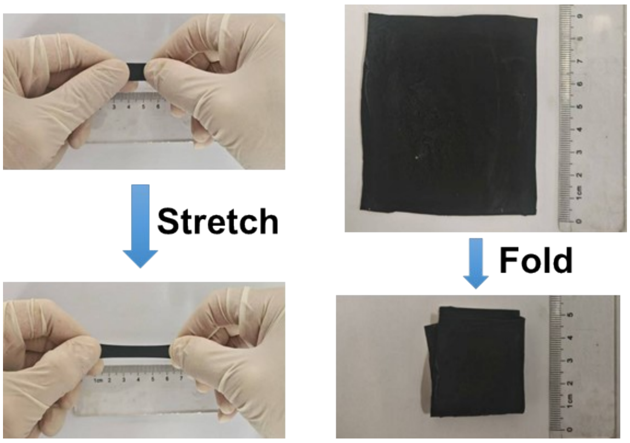

Fig. S8. Stretch, and fold of PVIL hydrogel, demonstrating that PVIL can be easily stretched and folded, showcasing its excellent flexibility.

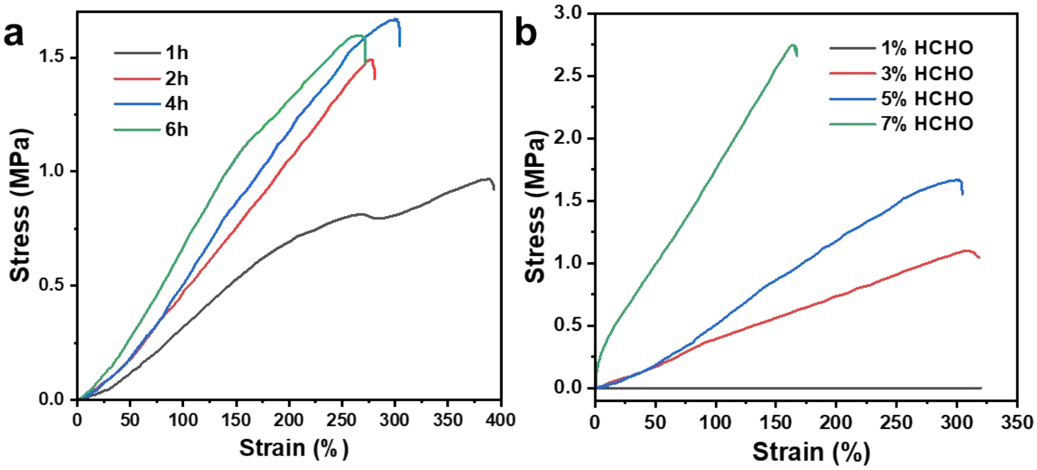

Fig. S9. Tensile stress-strain curves for PVIL hydrogels with, (a) different reaction time, (b) different HCHO content.

Fig. S9 illustrates the effects of varying aldol condensation times and different formaldehyde contents on the mechanical properties of PVIL hydrogels. With increasing reaction time, the cross-linking reaction proceeds toward completion, resulting in optimal mechanical performance after 4h, as depicted in **Fig. S9a**. Variations in HCHO content significantly affect the properties: as the concentration increases from 1% to 7%, the tensile strength rises from 0 MPa to 2.7 MPa, while the elongation at break decreases from 320% to 150%, as shown in **Fig. S9b**. This behavior is attributed to the enhanced cross-linking density of PVA, which restricts polymer chain mobile.

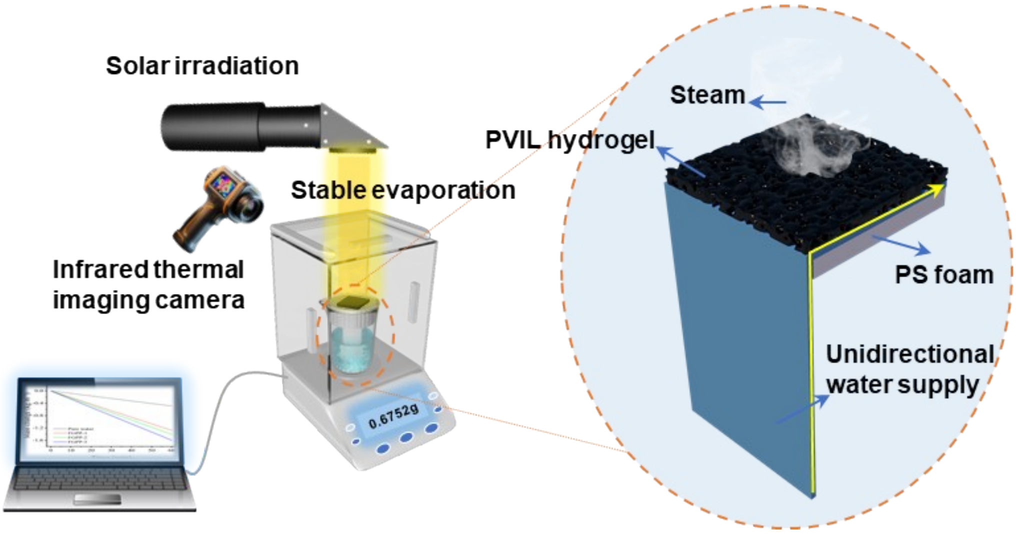

Fig. S10 Schematic diagram of solar-driven interfacial evaporation test setup and the constitution of platform evaporator

A solar-driven water evaporation experimental platform was constructed in the laboratory, as shown in **Fig. S10**. This platform comprises PVIL hydrogel, absorbent paper, and foam. A 2 cm slit was cut through the center of the foam, into which the absorbent paper was inserted. Its lower end was placed in contact with water, while its upper end was laid flat across the foam from left to right, establishing a unidirectional water supply channel. The PVIL was placed above the absorbent paper. An electronic balance recorded the mass loss of the PVIL hydrogel at each time point. An infrared thermal imaging camera documented the surface temperature distribution throughout the evaporation process.

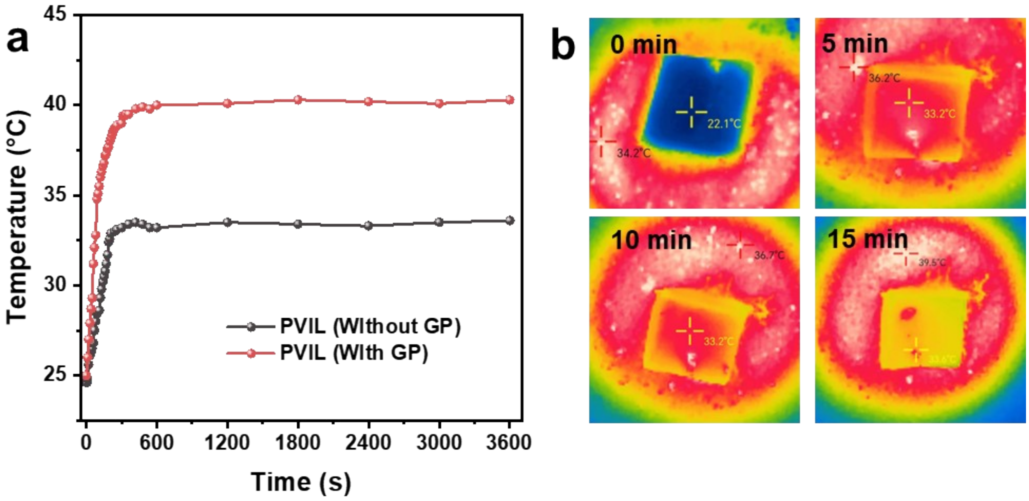

Fig. S11. (a) Temperature increase of PVIL hydrogel evaporator under 1-sun irradiation. (b) Thermographic sequence images of PVIL hydrogel (without GP) under 1- sun irradiation.

Fig. S11 displays the heating curves and infrared thermal imaging of samples with and without GP. It can be observed that the PVIL hydrogel without GP reaches a maximum temperature of only 33.6°C under 1-sun irradiation, whereas the GP-containing hydrogel exhibits a temperature of 41.4°C, confirming the excellent photothermal conversion performance of GP.

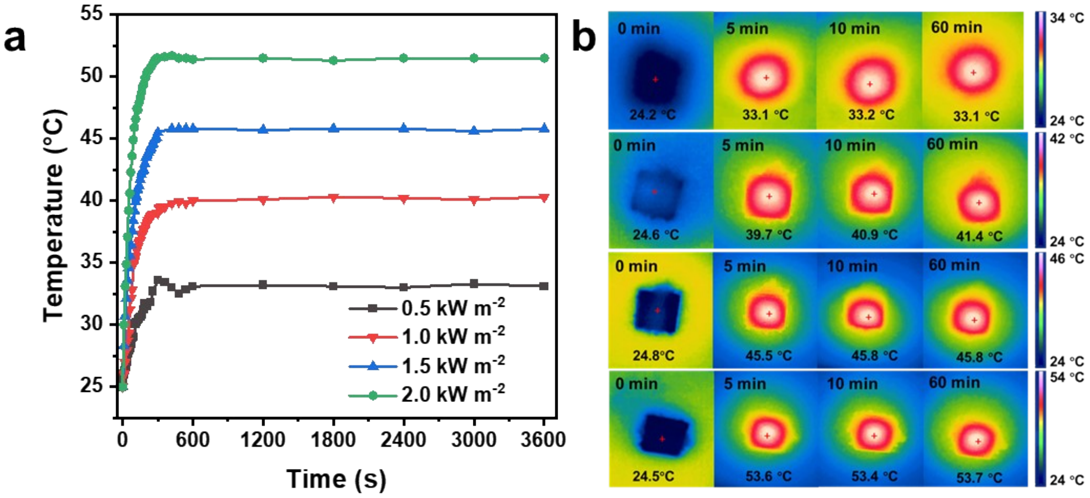

Fig. S12. (a) Temperature increase of PVIL hydrogel evaporator under different solar light intensities. (b) Thermographic sequence images of PVIL hydrogel evaporator under different solar light intensities.

Fig. S12 presents infrared thermal imaging of PVIL under varying light intensities. As light intensity increases, the PVIL hydrogel reaches final temperatures of 33.1, 41.4, 45.8, and 53.7°C after 1 h at 1-sun irradiation.

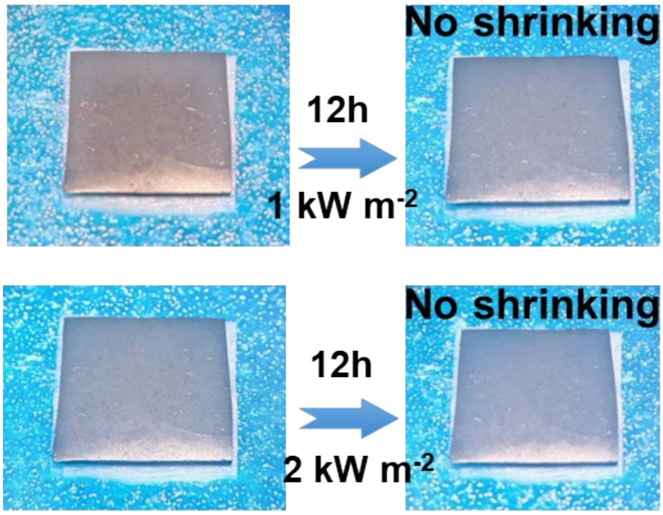

Fig. S13. Optical images of PVIL before and after 12 h of illumination at 1-sun irradiation.

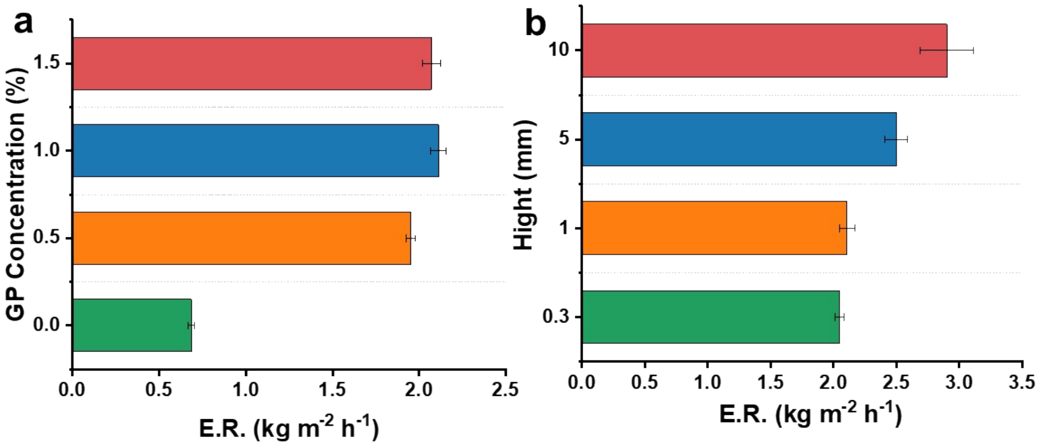

Fig S14. Evaporation rates of PVIL hydrogel at: (a) different GP content, (b) different exposure height.

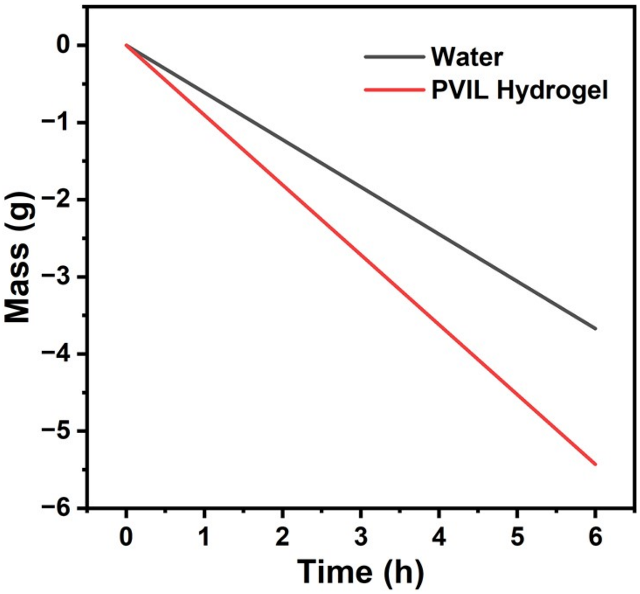

Fig. S15. PVIL hydrogel and pure water were placed in a 41 °C environment for 6 h, with mass changes over time.

To quantitatively evaluate the vapor generation behavior, the evaporation enthalpy of water within the PVIL hydrogel was investigated and compared with that of pure water. The measurement was conducted by placing samples with an identical surface area (2 cm× 2cm) in an oven at 41 °C, which is the steady-state surface temperature of the PVIL hydrogel under 1 sun illumination for 6 h. The mass loss of pure water was 3.6715 g, whereas the PVIL hydrogel exhibited a significantly higher mass loss of 5.4288 g over the same period **(Fig. S15)**. Based on this calculation, the evaporation enthalpy of water in the PVIL hydrogel was determined to be 1627 J g^{-1}.

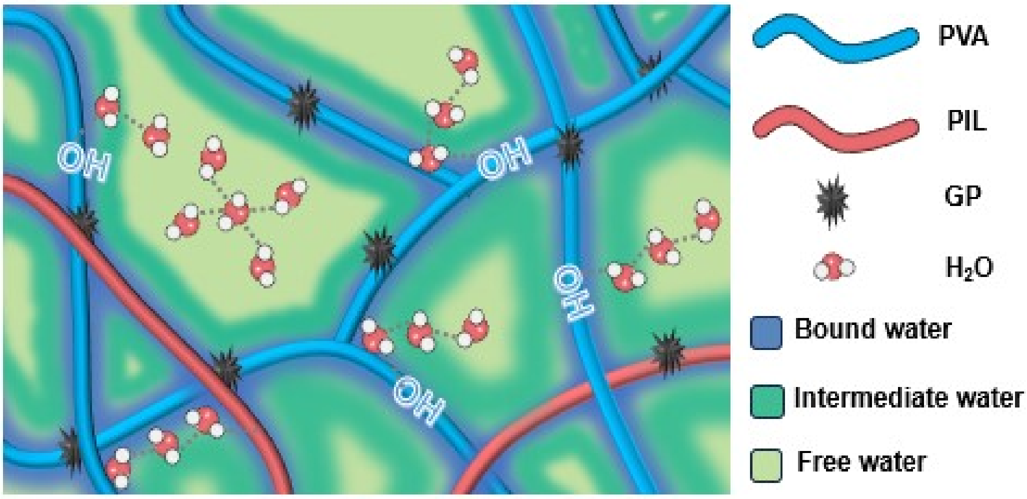

Fig. S16. The interfacial water molecular state of PVIL hydrogel.

Fig. S16. depicts BW stabilized by strong hydrogen bonds with polar polymer groups (–OH), while FW retains a tetrahedral structure with minimal polymer interaction. IW, a metastable intermediate with weakened hydrogen bonds, evaporates easily due to its proximity to the photothermal interface.

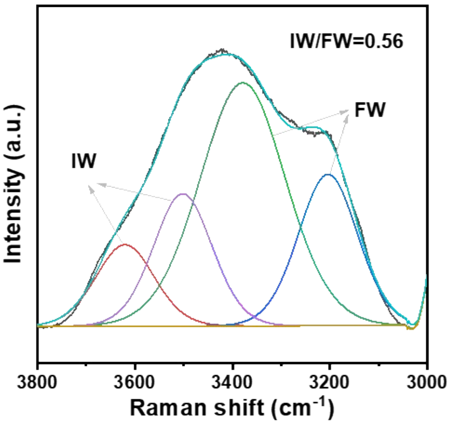

Fig. S17. Raman spectra and corresponding fitted curves of PVIL hydrogel.

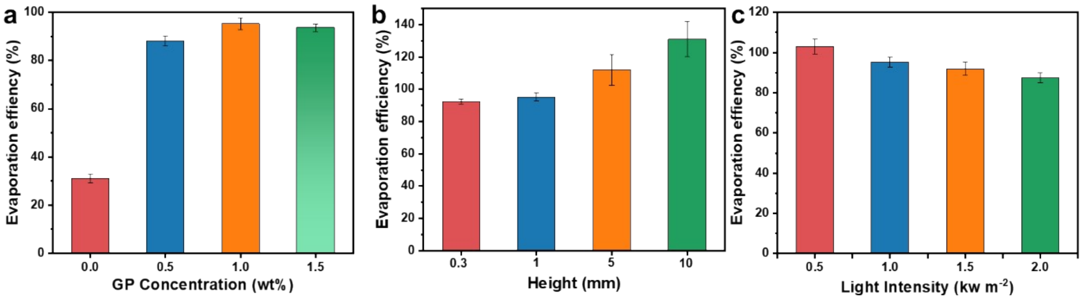

Fig. S18. Evaporation efficiency of PVIL under different conditions, (a) different GP content, (b) different exposure height, (c) different solar light intensities.

The evaporation efficiency of the PVIL hydrogel was systematically optimized by tuning key parameters **(Fig. S18)**. The evaporation rate increases with GP content up to 1.5% before plateauing **(Fig. S18a)**. A dramatic enhancement in efficiency was observed with increased height, reaching 131% at 10mm **(Fig. S18b)**. While higher light intensities produced higher surface temperatures, the corresponding evaporation efficiency decreased **(Fig. S18c)**. This indicates a greater proportion of energy is lost as heat (e.g., through radiation and convection) at higher power inputs.

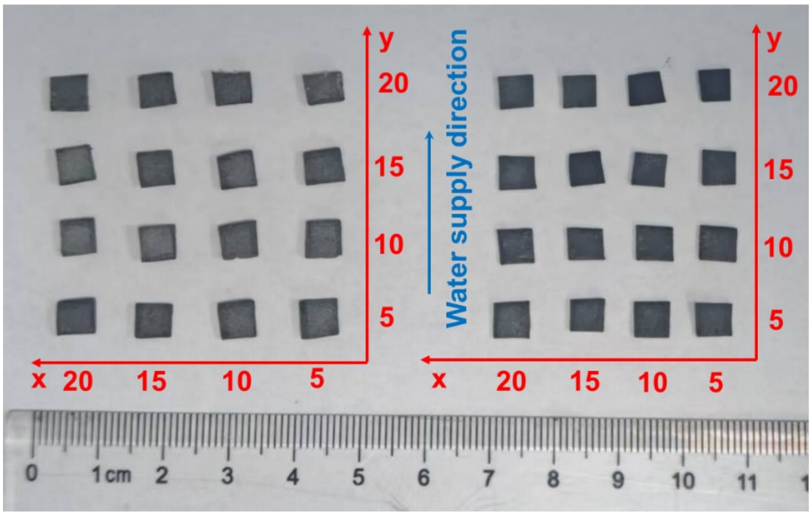

Fig. S19. Schematic of the 2 cm × 2 cm P and PVIL hydrogel cut into 16 equal pieces.

After 10 h of continuous illumination under 1 sun, the pristine P and PVIL hydrogels (2 cm × 2 cm each) were carefully removed and cut into 16 equal pieces following a predefined grid. The resulting fragments were labeled. Each piece was then immersed in 8 mL of deionized water for salt extraction. By analyzing the leachate concentration, the salt content in each fragment was accurately determined, enabling visualization of the salt distribution within the hydrogels

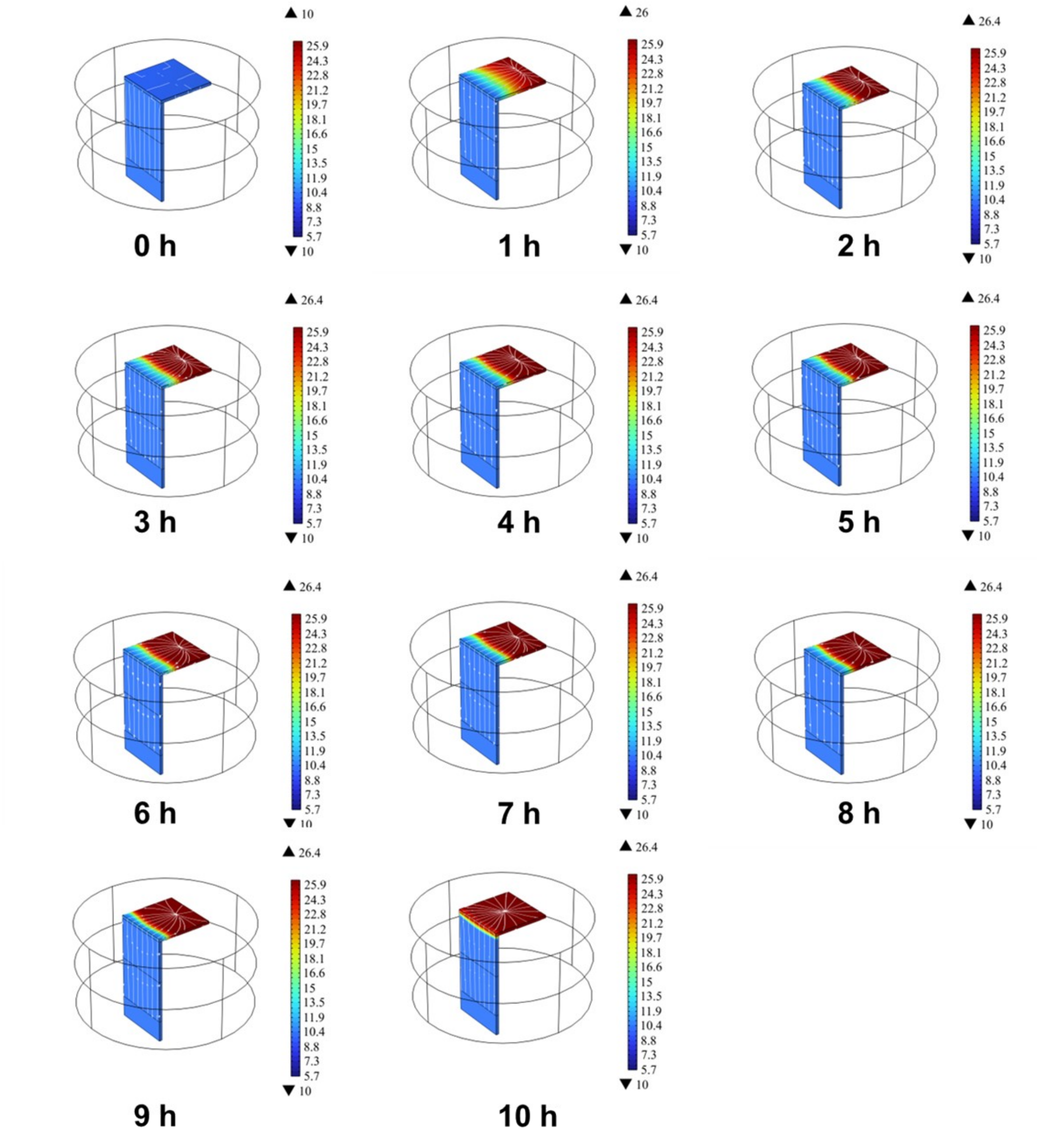

Fig. S20. Numerical simulation of salinity distribution of P hydrogel at different time.

Fig. S20 displays 3D simulated salt concentration distributions in P hydrogel during evaporation at varying time intervals (0–10 h). The color scale represents salt concentration (wt%), spanning from 10 (cool blue, low concentration) to 26.4 (warm red, saturation limit). At 0 h, the salt concentration is uniformly distributed across the entire hydrogel. From 1 to 3 h, a sharp concentration gradient emerges: the surface concentration increases rapidly. By 4 h, the surface concentration reaches the saturation limit (26.4 wt%), as indicated by the uniform red coloration on the P hydrogel's top surface. From 4 to 10 h, the saturated surface region expands and stabilizes. These results highlight the rapid surface salt enrichment and early saturation kinetics of P hydrogel during evaporation. The timely attainment of surface saturation (by 4 h) and the persistent concentration gradient between the surface and inner bulk are critical for understanding the material's performance in applications such as desalination, where controlled salt accumulation and release are essential.

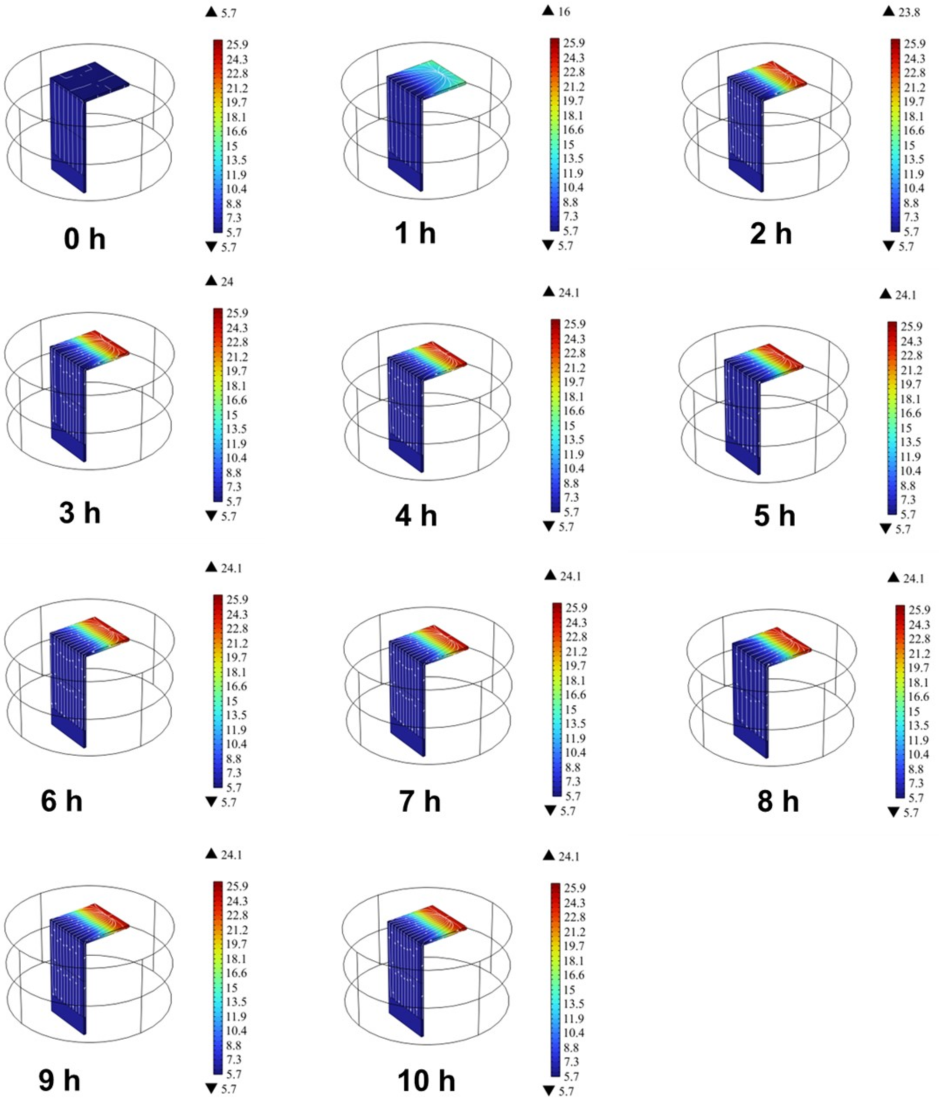

Fig. S21. Numerical simulation of salinity distribution of PVIL hydrogel at different time.

Fig. S21 shows simulated salt concentration distributions in PVIL hydrogel during 0–10 h evaporation. The PVIL hydrogel starts with a During early evaporation (0–3 h), PVIL exhibits slower surface enrichment: at 1 h, its surface concentration reaches 16 wt.% (vs. ~26 wt.% in P hydrogel), and by 3 h, it reaches 24 wt.% (vs. near-saturation in P hydrogel). Notably, the pristine P hydrogel achieves full surface saturation (26.4 wt.%) by 4 h, maintaining a sharp surface-bulk gradient, whereas PVIL remains sub-saturated (<25 wt.%) throughout 10 h with a milder gradient. These results indicate that the PIL-induced Donnan effect in PVIL alters the microenvironment within the hydrogel, thereby delaying salt enrichment and inhibiting saturation. Such controlled salt distribution is advantageous for desalination, where rapid surface scaling degrades performance, highlighting PVIL hydrogels’ potential for sustainable water applications.

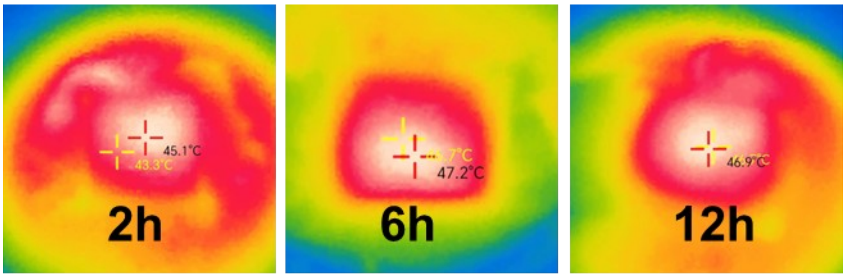

Fig. S22. Thermographic sequence images of PVIL hydrogel at different time points during the 10wt% NaCl test.

The infrared thermal images in **Fig. S22** captured at 0 h, 6 h, and 12 h under 1-sun irradiation demonstrate a remarkably stable surface temperature, maintains at approximately 47 °C throughout the test.

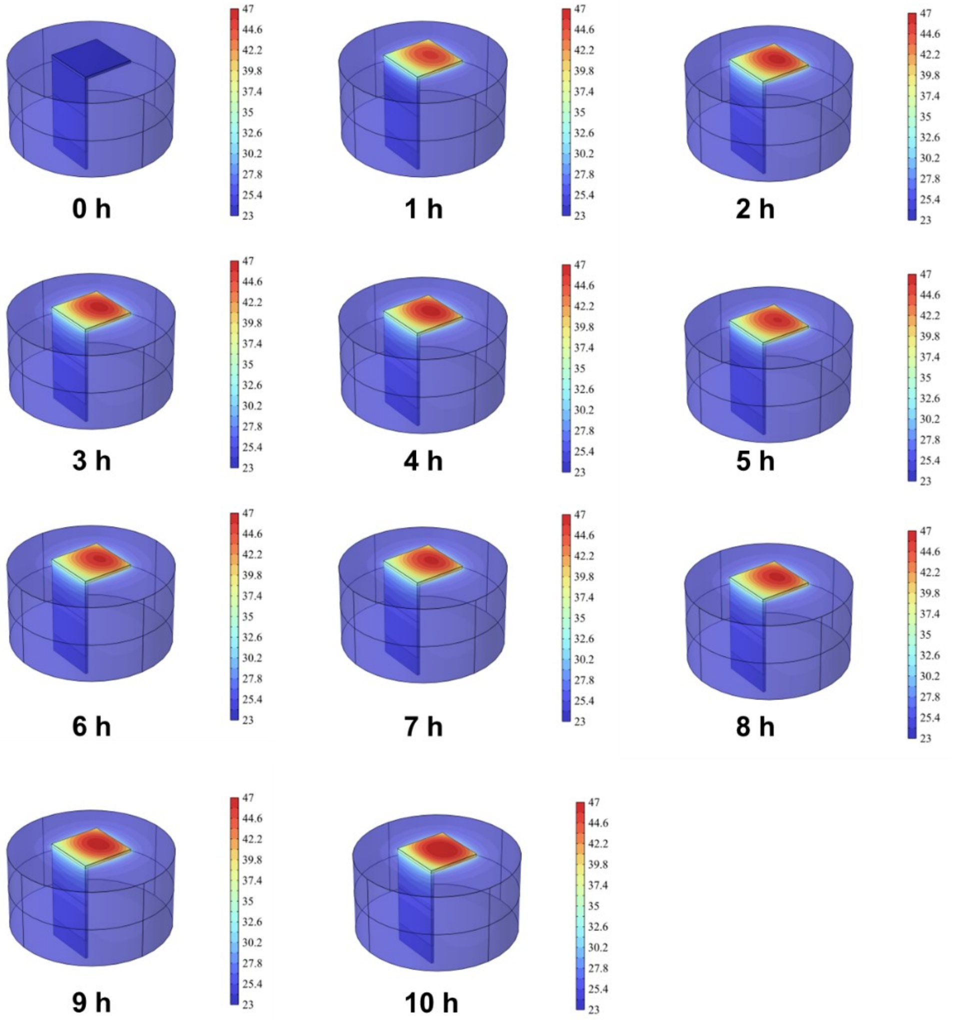

Fig. S23. Numerical simulation of Temperature distribution of P hydrogel at different time.

Fig. S23 simulates the temperature distribution of the P hydrogel during evaporation, with the highest temperature (47 °C) occurring at the center. Temperatures are slightly lower near the water supply side.

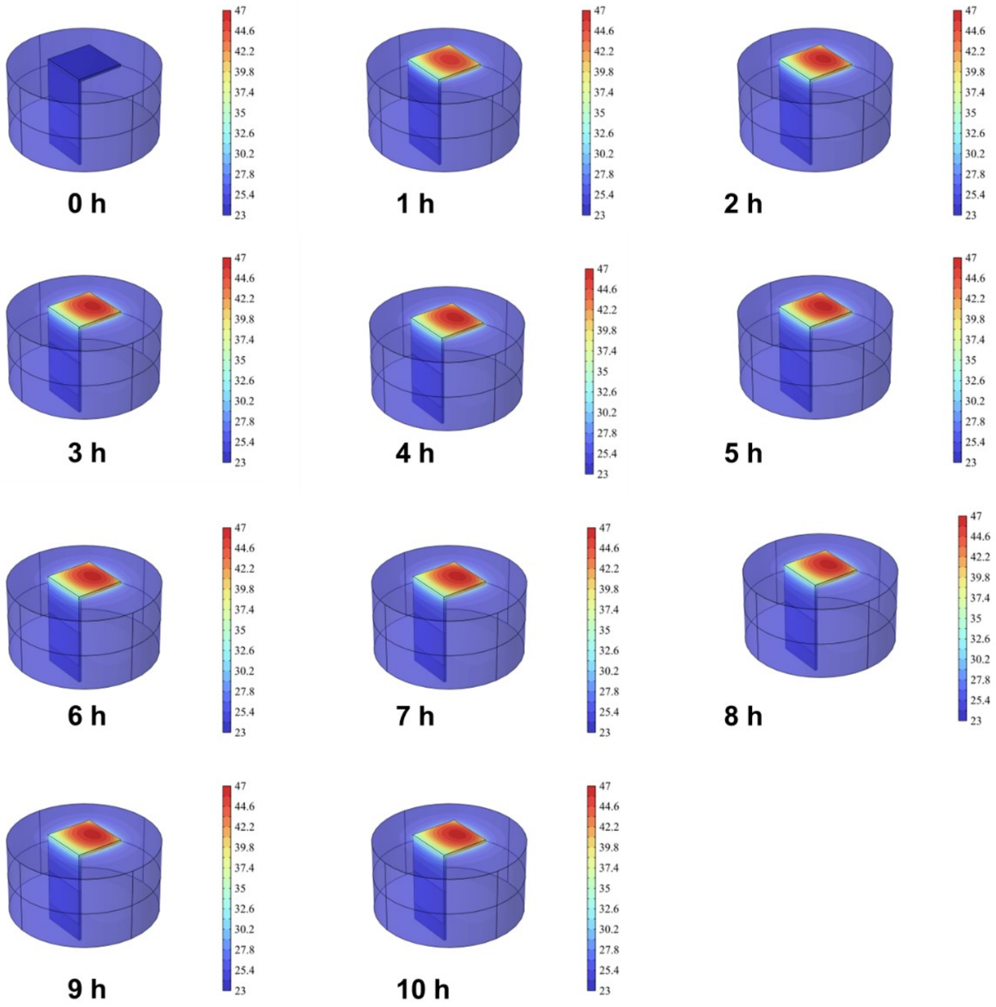

Fig. S24. Numerical simulation of Temperature distribution of PVIL hydrogel at different time.

Fig. S24 represents the simulated temperature distribution of the PVIL hydrogel during evaporation. Similar to the P hydrogel, the central region exhibits the highest temperature (47 °C). Temperatures near the water supply side are slightly lower. Furthermore, the simulated temperatures closely resemble those observed during actual testing.

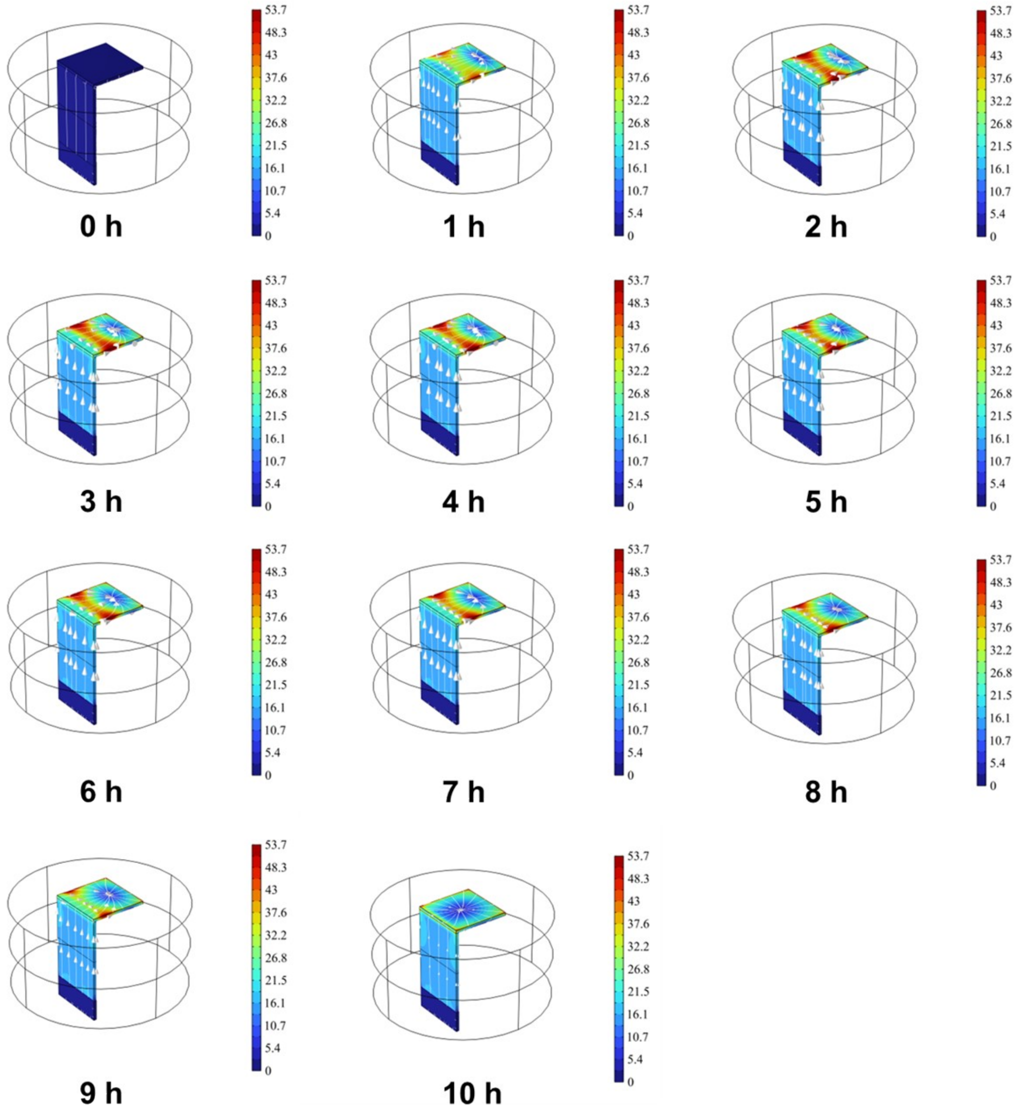

Fig. S25. Numerical simulation of flow velocity (unit: μm/s) distribution of P hydrogel at different time.

Fig. S25 presents simulated velocity distributions of pristine P hydrogel during 0–10 h evaporation, where the color scale (0 to 53.7 μm/s) quantifies Marangoni convection intensity, driven by surface tension gradients from evaporation-induced temperature and concentration differences. Uniformly low velocity (<10 μm/s) across the hydrogel, as no surface gradients exist prior to evaporation (0 h).Velocity increases sharply at the evaporation surface (20–40 μm/s), forming distinct convection cells due to emerging surface tension gradients (from localized evaporation, 1-3 h).Velocity peaks at the surface center (~50 μm/s), reflecting a maximum in surface tension driving force balanced by viscous resistance. The gradient between the high-velocity surface (30–50 μm/s) and low-velocity bulk (<20 μm/s) becomes pronounced (3-6 h). Over 6–10 hours, the velocity gradually decreased. Due to the accumulation of surface salts, the salinity gradient at both ends progressively diminished, and the Marangoni convection effect did not further intensify.

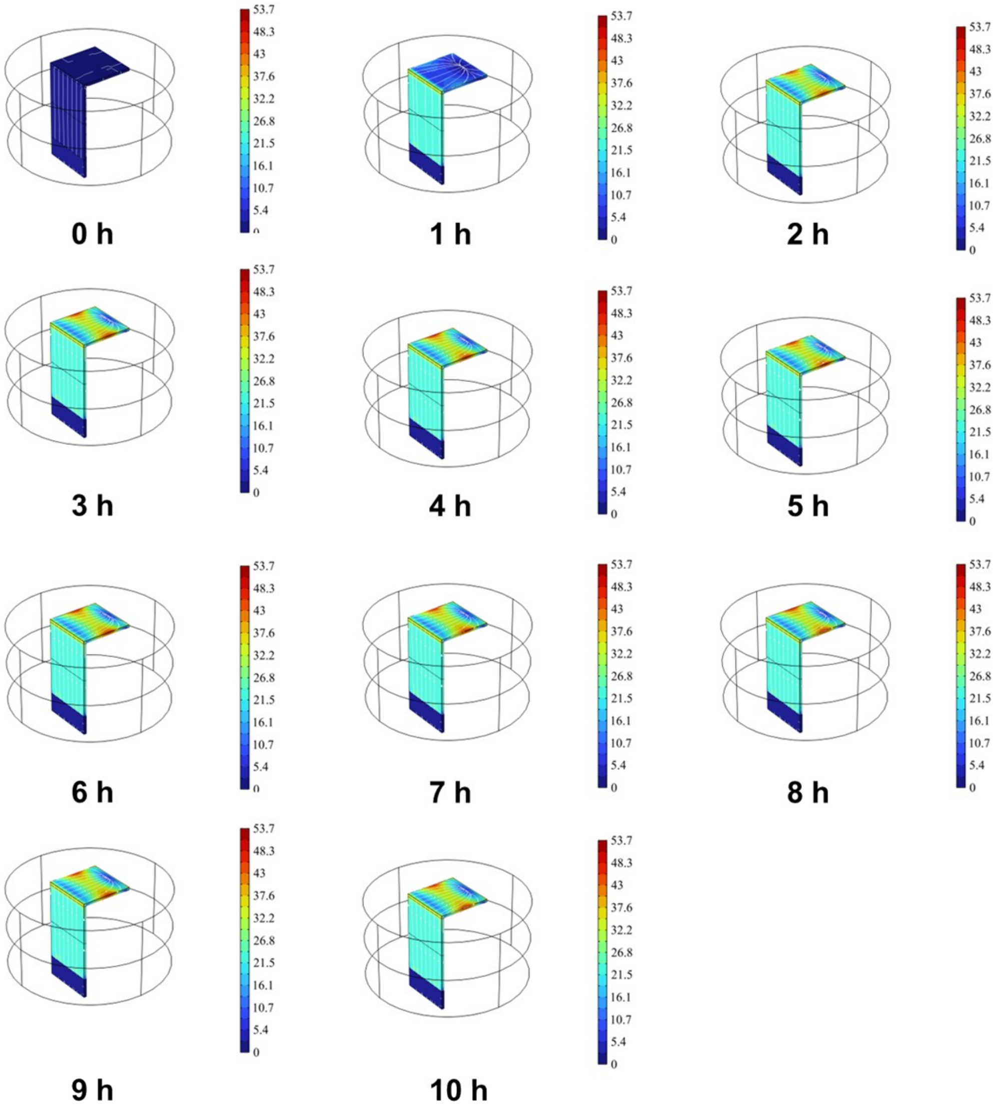

Fig. S26. Numerical simulation of flow velocity (unit: μm/s) distribution of PVIL hydrogel at different time.

Fig. S26 depicts simulated velocity distributions of PVIL hydrogel during 0–10 h evaporation, where the color scale (0 to 53.7 μm/s) quantifies Marangoni convection intensity, driven by surface tension gradients from evaporation-induced temperature/concentration differences. 0 h: Uniformly low velocity (<10 μm/s) due to negligible surface gradients before evaporation. 1–2 h: Velocity increases markedly at the evaporation surface (~30–40 μm/s), forming distinct convection cells as surface tension gradients develop. 3–5 h: Velocity stabilizes with a peak intensity (~50 μm/s) at the surface center, reflecting a balance between evaporation, driven gradients and viscous damping. 6–10 h: Velocity remains consistent (30–50 μm/s), indicating a quasi-steady state where Marangoni convection sustains mass transport (water evaporation, salt migration) without further intensification.

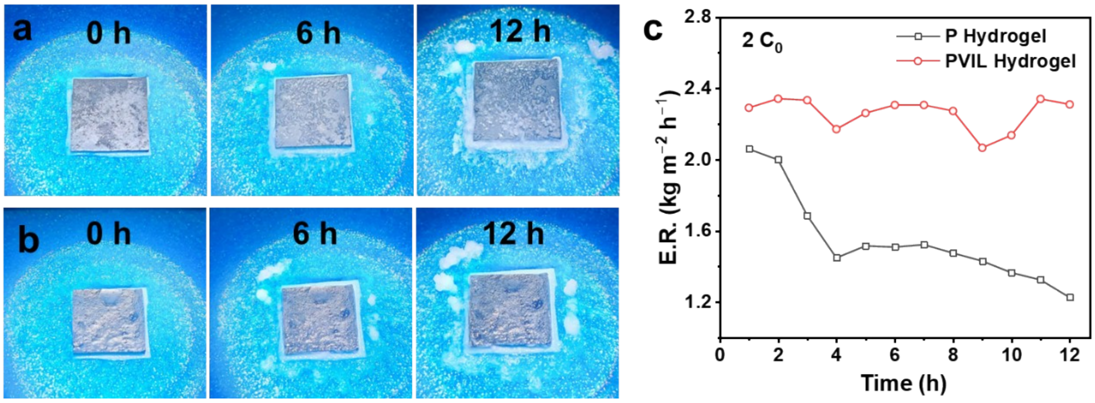

Fig. S27. Optical photographs of (a) P hydrogel and (b) PVIL hydrogel during 12 h of continuous solar evaporation in 2× concentrated seawater under 1 sun illumination. (c) The corresponding evaporation rates of P and PVIL hydrogels over the 12 h testing in 2× concentrated seawater.

Continuous evaporation tests in 2× concentrated seawater (2 C_0) were conducted to evaluate long-term anti-fouling stability. As shown in **Fig 27a** and **b**, P hydrogel suffered severe surface salt scaling after 12 h, leading to a drastic decline in its evaporation rate due to the blockage of vapor escape channels **(Fig. 27c)**. In stark contrast, the PVIL hydrogel maintains a pristine, salt-free surface and a highly stable evaporation rate throughout the entire testing period. This remarkable difference firmly validates our synergistic anti-fouling design: rather than relying solely on physical capillary transport which easily gets overwhelmed by high salt fluxes (as seen in the P hydrogel), the charged network in the PVIL hydrogel exerts a robust Donnan exclusion effect. This chemical pre-screening substantially restricts the initial influx of scaling ions at the water-pumping interface, fundamentally alleviating the burden on subsequent lateral geometric transport and ensuring stable zero-liquid-discharge (ZLD) operation under hypersaline conditions.

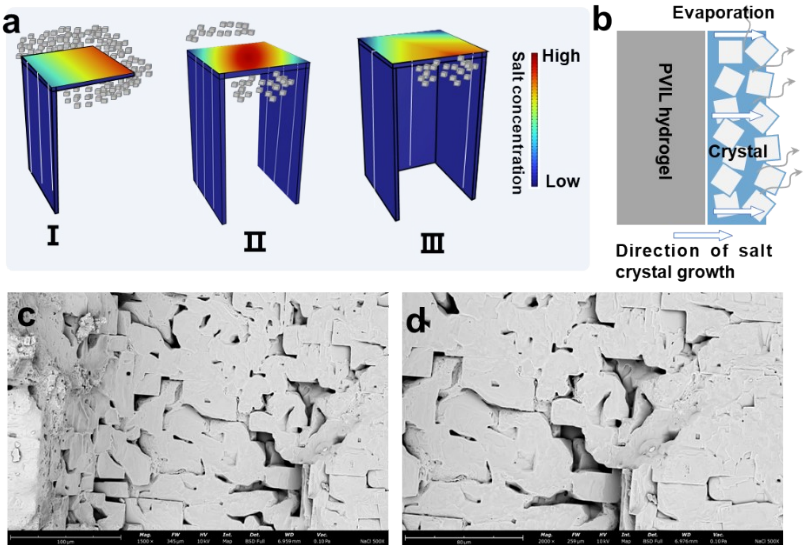

Fig. S28. (a) Schematic of final salt crystal distribution for the three configurations. (b) Schematic of edge-preferential salt crystallization on the PVIL hydrogel. (c, d) SEM images of the collected salt from PVIL hydrogel edge at different magnifications.

Fig. S28 presents SEM images of edge salt crystallization in PVIL hydrogel, revealing well-defined cubic salt crystals with a hydrophilic, porous structure. The cubic morphology typical of crystalline salts (NaCl), and porous, hydrophilic nature of the crystals provide abundant sites for water adsorption and facilitate ion diffusion. The hydrophilic PVIL hydrogel ensures sufficient water supply to the edge region (where evaporation rates are inherently higher), maintaining a stable ion concentration gradient that drives salt migration from the hydrogel bulk to the edge. This, coupled with the hydrophilic surface of the crystals, promotes continuous salt nucleation and growth. The porous structure further enhances ion transport, accelerating crystallization kinetics. Importantly, the sufficient water supply and hydrophilic interactions between the hydrogel and salt crystals enable continuous salt formation and growth, resulting in a higher salt yield compared to systems with non-hydrophilic hydrogels or limited water availability.

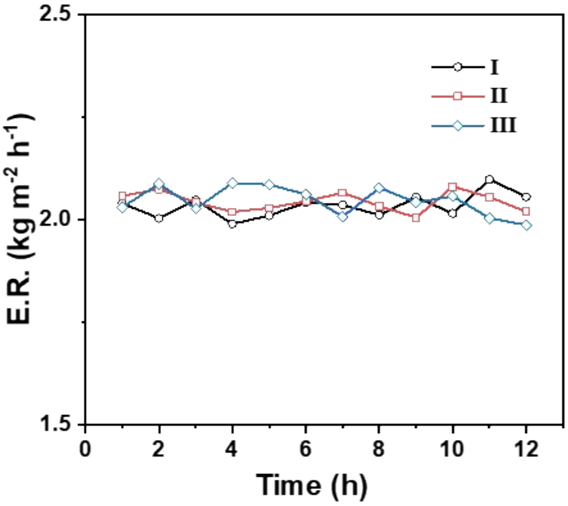

Fig. S29. Evaporation rates over 12 h of three water-supply modes.

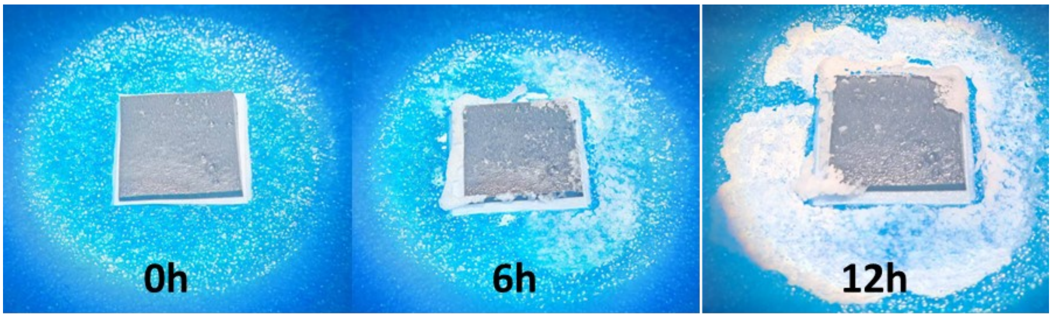

Fig. S30. Optical images of P hydrogel evaporation at 0 h, 6 h, and 12 h under three water supply pathways.

As shown in **Fig. S30**, salt crystallization occurred on the P hydrogel evaporating in 10 wt.% NaCl with a single water channel. In contrast, no crystallization was observed when three water channels were employed. This result demonstrates that the multi-channel design effectively prevents salt accumulation. The additional channels create shorter, more efficient pathways for ion transport. This ensures rejected salt ions are efficiently dispersed back into the bulk solution, preventing localized supersaturation and thereby inhibiting crystal formation. This simple structural modification is key to maintaining stable evaporation in high-salinity brines.

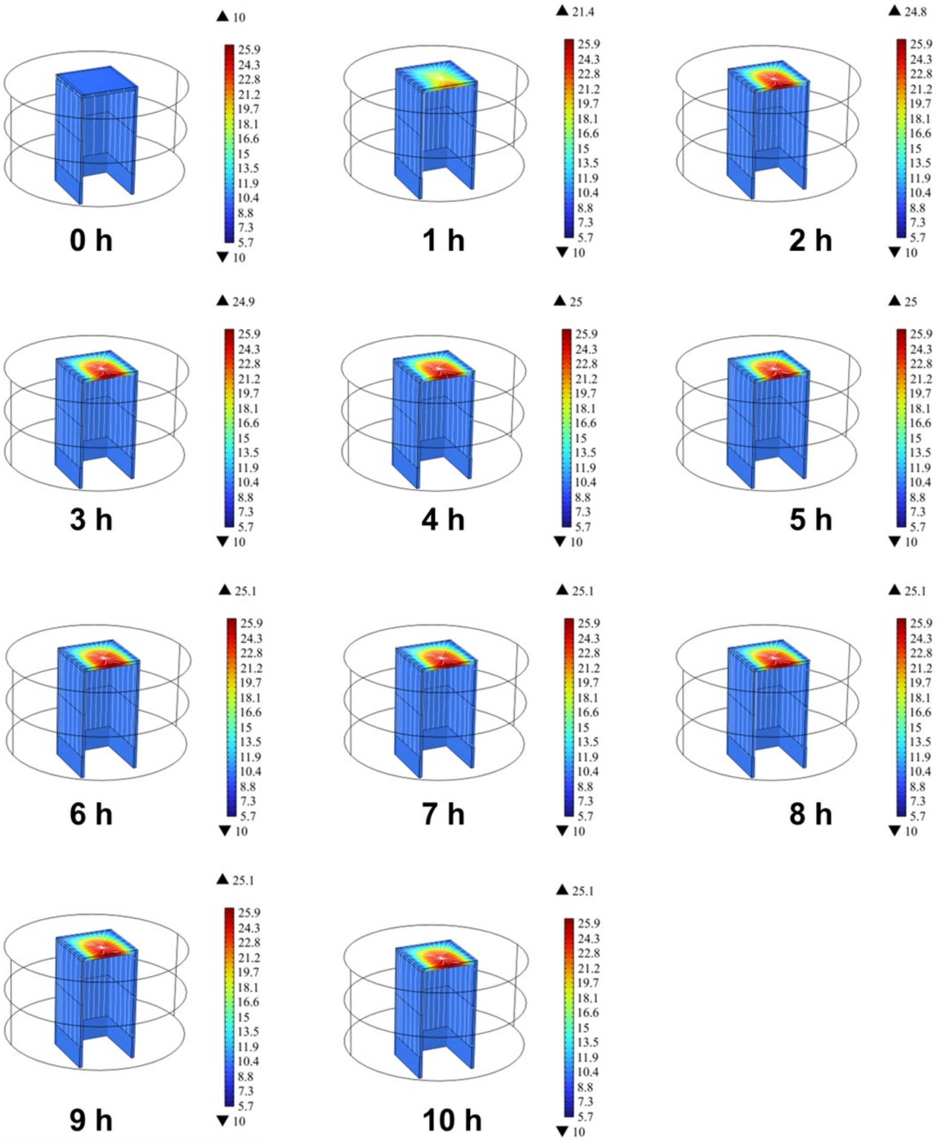

Fig. S31. Numerical simulation of internal salinity distribution in P hydrogel at different time under a three-channel water supply mode.

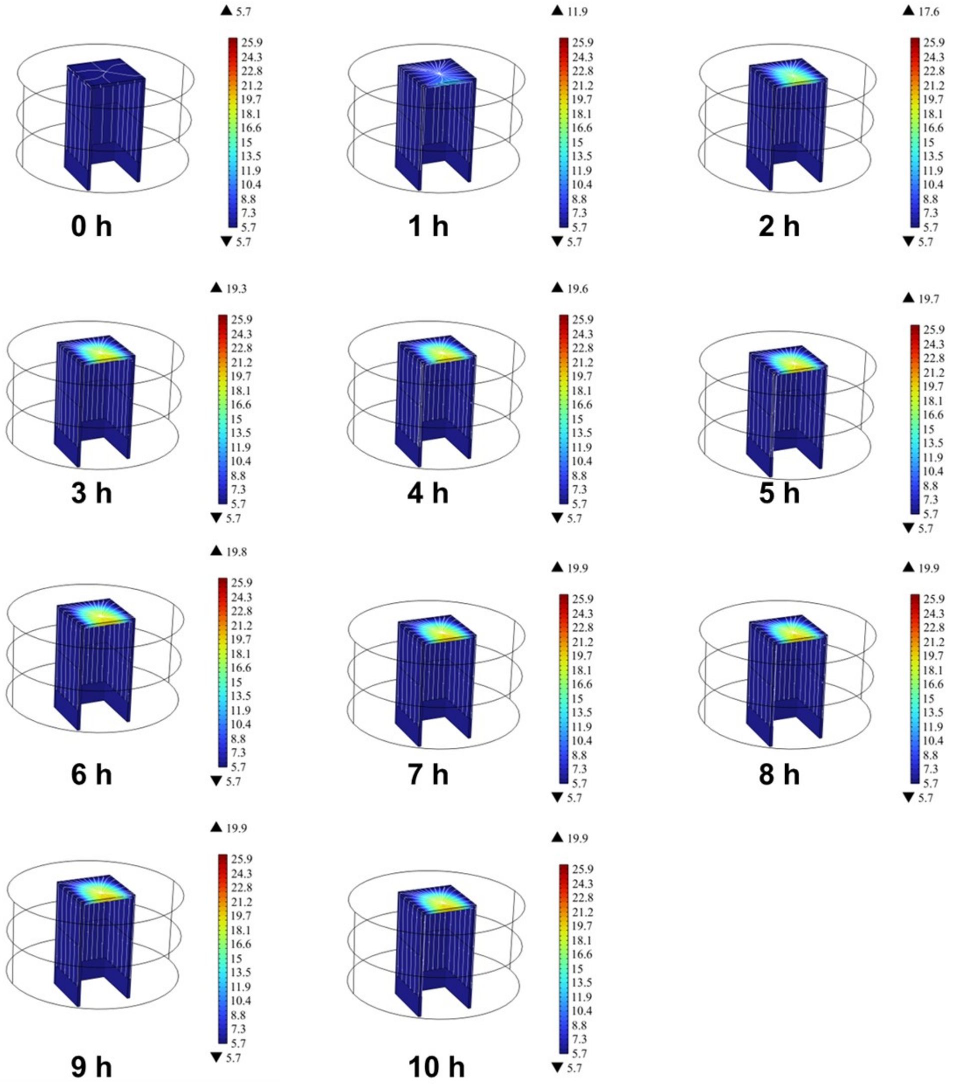

Fig. S32. Numerical simulation of internal salinity distribution in PVIL hydrogel at different time under three-channel water supply modes.

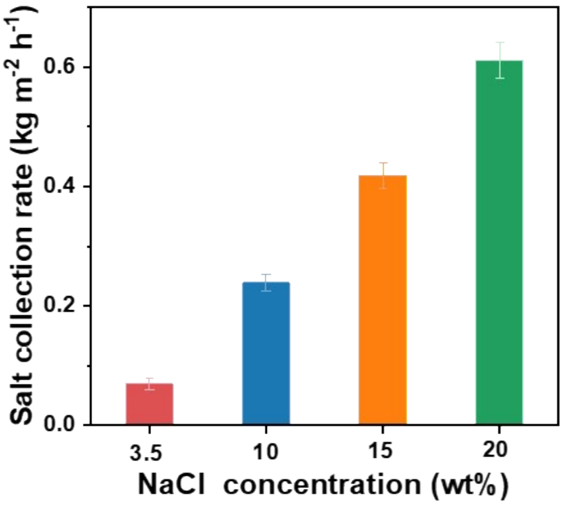

Fig. S33. Salt collection rate by the PVIL hydrogel from different NaCl concentration under 1-sun irradiation.

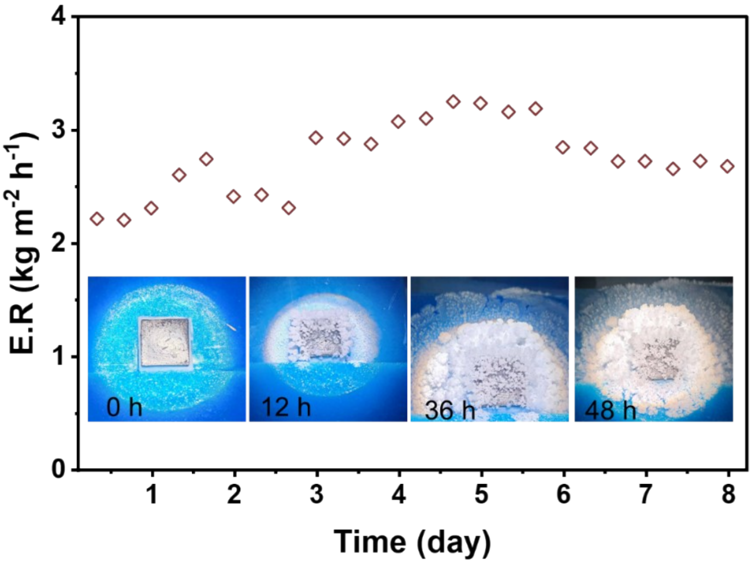

Fig. S34. Long-term evaporation performance of the PVIL hydrogel in a 20 wt% NaCl solution over 8 days. The inset shows optical photographs of the hydrogel surface at 0 h, 12 h, 36 h, and 48 h.

As shown in **Fig. S34**, when the PVIL hydrogel is tested in 20 wt% brine, the evaporation rate does not decrease but instead shows an increase. This is attributed to the fact that although optical photographs show the PVIL surface covered with salt, these salts are extremely loose and hydrophilic. The presence of such loose salts increases the effective evaporation area of the hydrogel, which in turn leads to a rise in the evaporation rate. These experimental results demonstrate the potential of the PVIL hydrogel for treating high-salinity water.

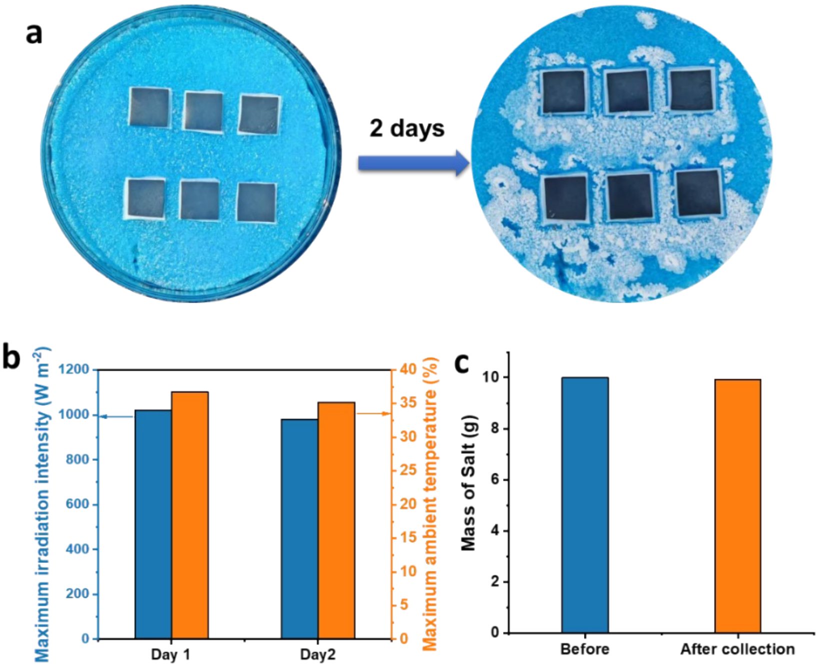

Fig. S35. (a) Optical picture of an array evaporator comprising six PVIL hydrogels before and after 2 days of evaporation under natural light. (b) The maximum irradiation intensity and highest ambient temperature during 2 days of outdoor evaporation. (c) The salt content in the 100 g salt solution prior to evaporation and the mass of salt collected after evaporation.

To evaluate the real-world performance of the PVIL hydrogel-based solar evaporator, an outdoor experiment was conducted using six identical hydrogels (2 cm × 2 cm each) under natural sunlight. The system was initialized with 100 g of NaCl solution (10 wt% salinity). Over a two-day period, the PVIL hydrogels achieved complete evaporation of the brine, with salt crystals selectively deposited at the periphery of each hydrogel unit. Notably, the evaporative surfaces remained free of salt coverage, indicating effective salt rejection and prevention of fouling, a critical advantage for sustained operation **(Fig. S35a)**. Environmental conditions as illustrated in **Fig. S35b**, with a peak irradiation intensity of 1020 W m^{-2} and a maximum ambient temperature of 36.2°C. Salt collection and ZLD Post-evaporation, 9.92 g of NaCl was collected from the initial 10 g of salt input, yielding a salt recovery efficiency of 99% (**Fig. S35c**). This near-quantitative salt collection coupled with the absence of residual liquid confirms the system's capability to achieve ZLD.

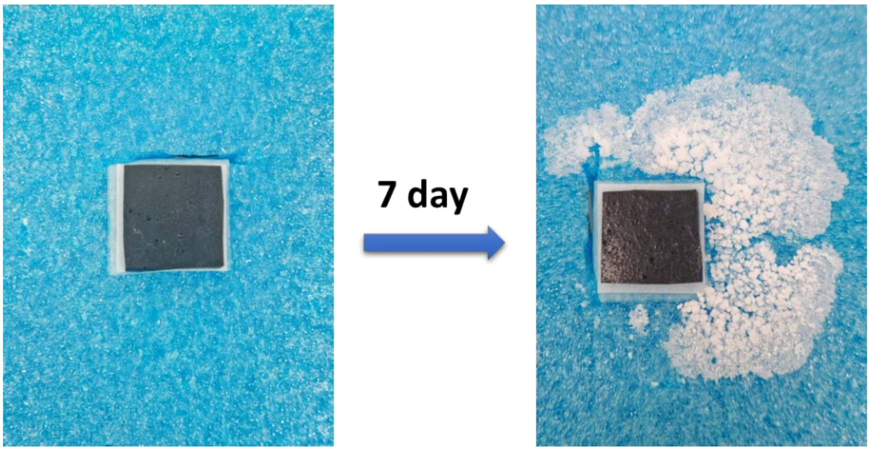

Fig. S36. Optical picture of salt crystallization in PIL hydrogel after seven days of evaporation under dark conditions (Temperature 25~26 °C, humidity 50~60%).

The PVIL was placed in an environment with a temperature of 25~26 °C and a relative humidity of approximately 50~60%, as shown in **Fig. S36**. Under dark conditions, salt crystallization was also achieved in the PVIL's three sides. This confirms the PVIL hydrogel's capability for salt production under all weather conditions.

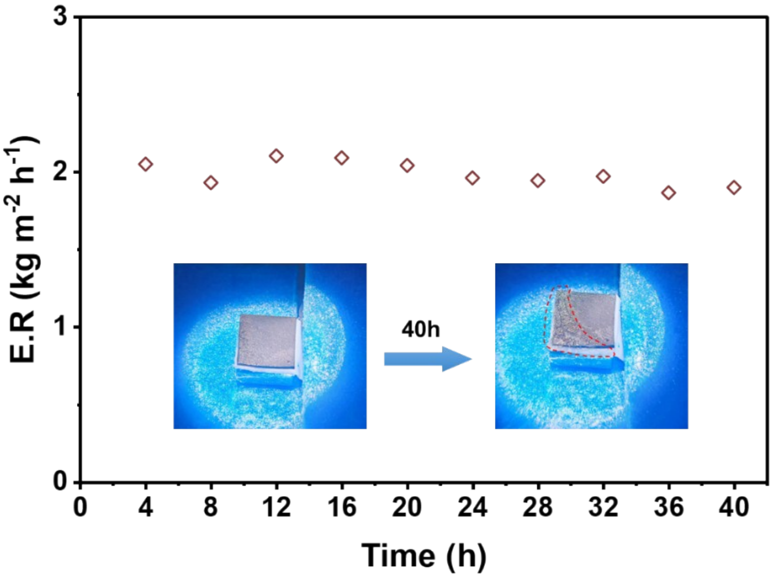

Fig. S37. Evaporation performance and salt crystallization behavior of the PVIL hydrogel in 3.5 wt% LiCl solution. The plots illustrate the evaporation rate over time, while the insets display optical photographs showing the progression of salt crystallization and the surface condition of the hydrogel at various intervals (0–40 h).

To evaluate the PVIL hydrogel's versatility as a reliable pre-treatment concentration platform for lithium-containing brines, the PVIL hydrogel is tested in a 3.5 wt% LiCl solution. The PVIL hydrogel maintains a stable and high evaporation rate throughout the operation. As shown in the **Fig. S37** optical images, LiCl crystals successfully precipitate and accumulate around the evaporator. Notably, after 40 hours of continuous operation, although lithium salts deposits partially on the evaporator surface, the physical state of the LiCl deposits differs significantly from that of NaCl. Due to the high hygroscopicity of lithium salts, the accumulated LiCl forms a loose, hydrated, and slush-like layer rather than a dense, hard crust. Consequently, this "wet" salt layer does not block the vapor escape channels or impair the porous structure of the hydrogel. Instead, it maintains a humid interface that sustains evaporation. Furthermore, this loose, hydrated salt is easily scraped off the surface, facilitating efficient collection. These results underscore the PVIL hydrogel's robust antifouling capability and its significant potential for achieving rapid volume reduction, efficient brine concentration, and subsequent salt crystallization.

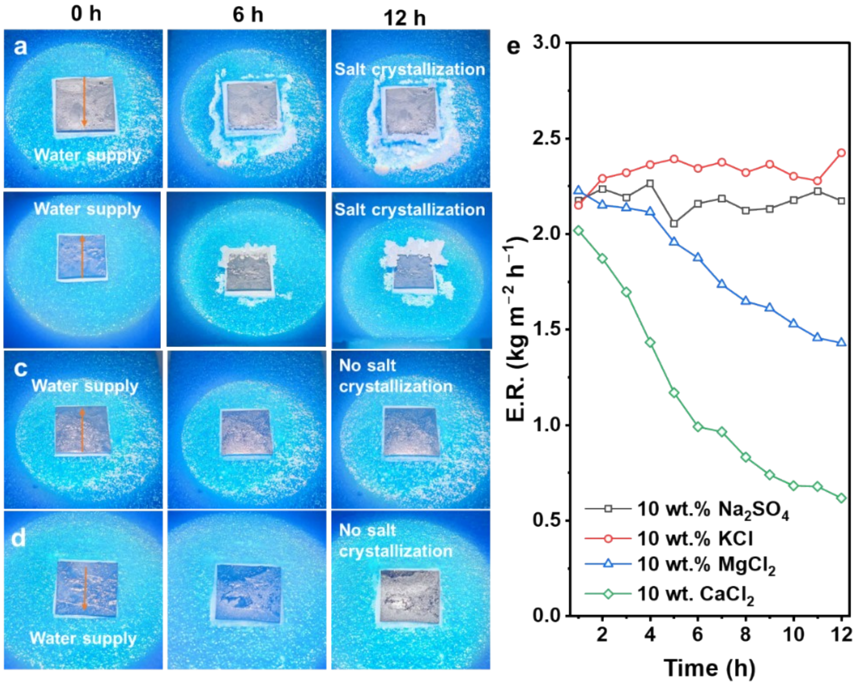

Fig. S38 Optical images of (a) Na_2SO_4, (b) KCl, (c) $MgCl_2$, and (d) $CaCl_2$ at different evaporation times. (e) Corresponding evaporation rates over time.

Fig. S38 highlights a clear ion-specific difference in crystallization location and evaporation consequence. For monovalent salt systems (e.g., Na_2SO_4 and KCl), salts are preferentially expelled to the outer surface/edge, where visible crystallization occurs, indicating that the internal transport channels remain open and the evaporation flux can be maintained. In contrast, for divalent salt systems (e.g., $CaCl_2$ and $MgCl_2$), little or no visible surface crystallization is observed, yet the evaporation rate declines sharply. This does not indicate antifouling, but rather a more detrimental failure mode in which divalent salts precipitate within the material and form dense internal scale/films that block water transport pathways. $MgCl_2$ is particularly severe because of its stronger hygroscopic/deliquescent nature, which further aggravates internal wet-salt blockage and flux decline. Therefore, the figure suggests that monovalent salts are more amenable to recovery via surface/edge crystallization, whereas divalent salts are more prone to induce internal mineral scaling, causing flux decay without obvious external salt precipitation, in agreement with the literature[1].

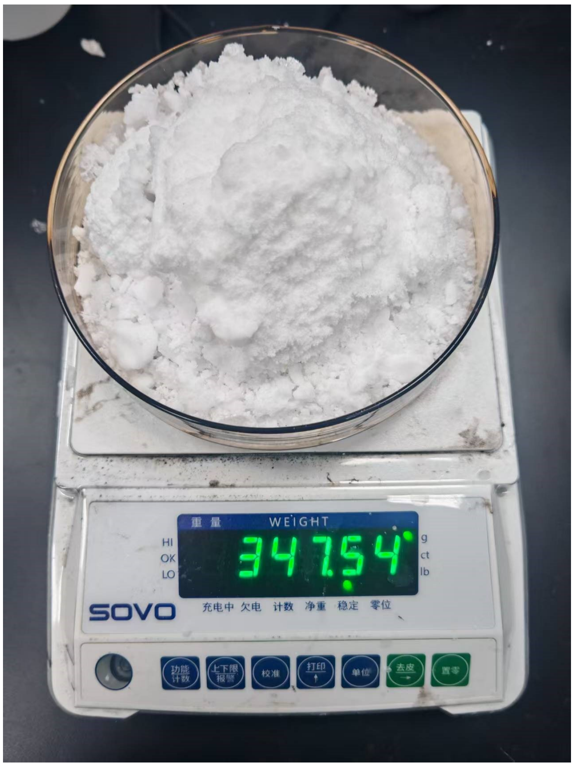

Fig. S39. Photograph of solid salt harvested after 152 days of evaporation in a 10 wt.% NaCl solution.

Fig. S39 illustrates the accumulated salt in a 2 cm×2 cm PVIL hydrogel sample after 152 days of evaporation in a 10 wt.% NaCl solution. The total mass was 347.54 g.

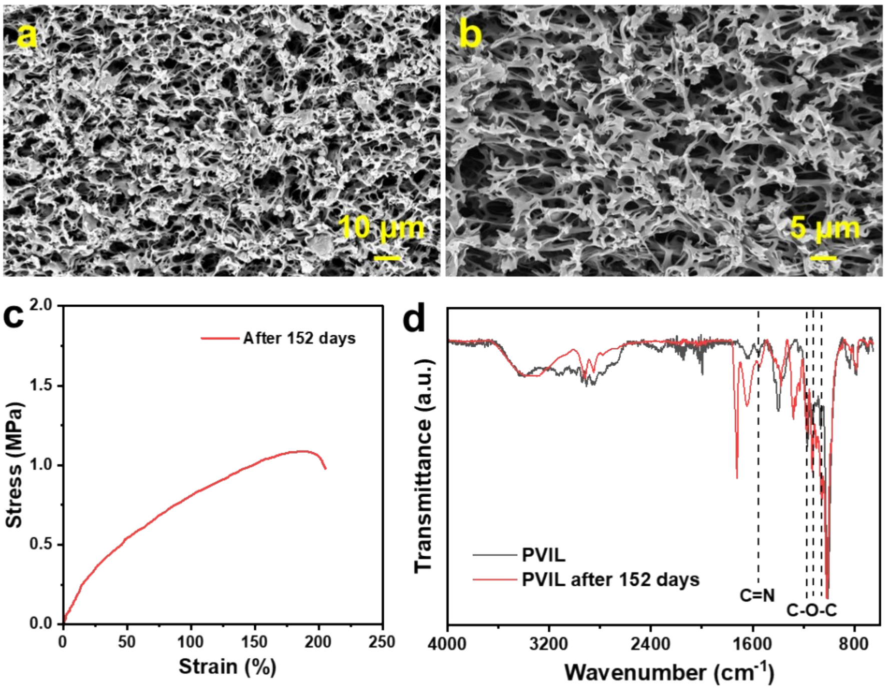

Fig. S40. Characterization of the PVIL hydrogel after 152 days of evaporation in 10 wt% NaCl solution. (a, b) SEM images under different magnification, (c) stress–strain curve, and (d) FTIR spectra.

After 152 days of continuous evaporation in 10 wt% NaCl solution, the PVIL hydrogel shows no significant change in microscopic morphology, as observed by SEM. The tensile strength remains close to 1 MPa, and the FT-IR spectra exhibits no noticeable shifts or new peaks, indicating excellent chemical and structural stability.

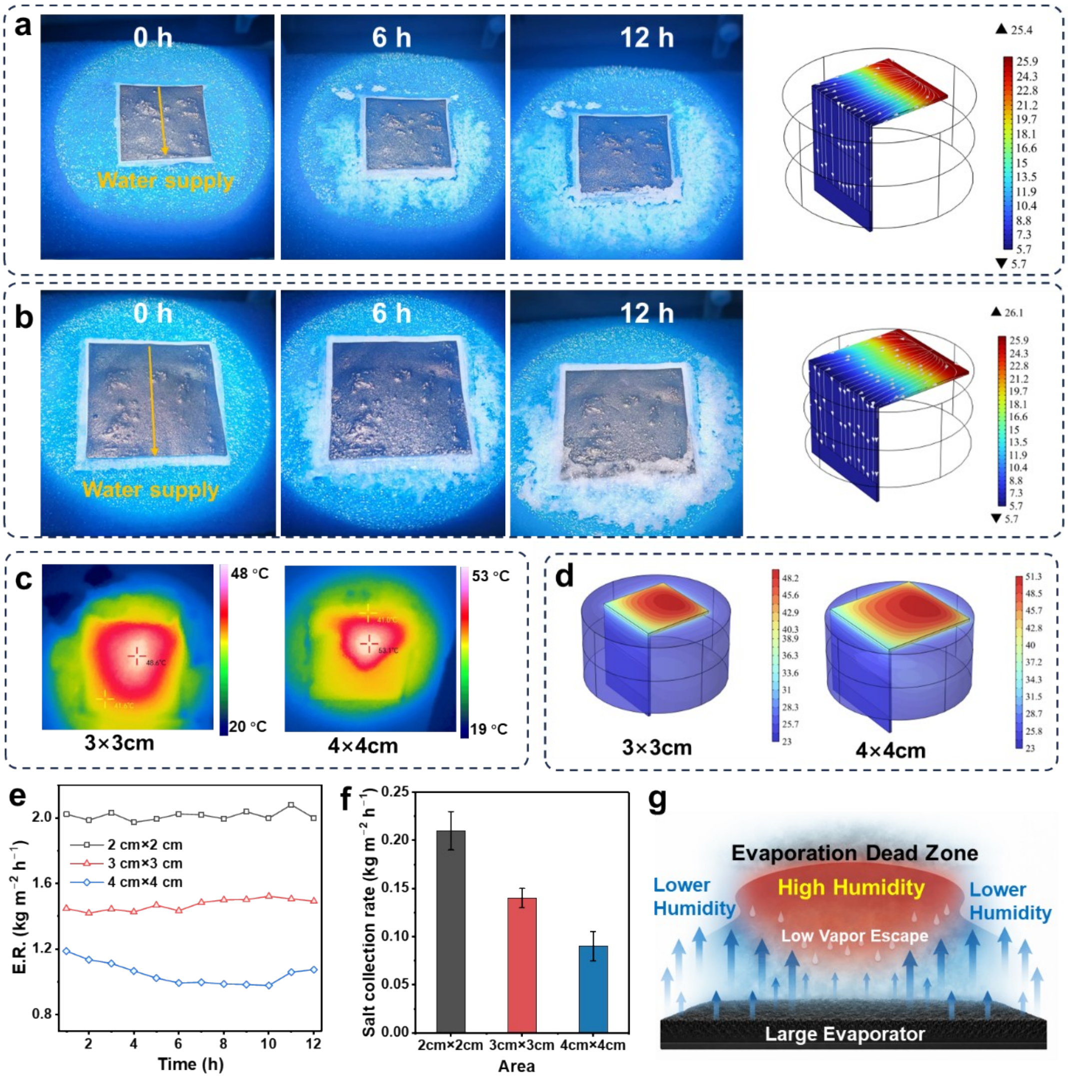

Fig. S41. (a-b) Optical photographs monitoring the continuous evaporation process over 12 h in 10 wt% NaCl solution and the corresponding COMSOL multiphysics simulations of the steady-state internal salt concentration distribution for monolithic samples sized at (a) 3 cm×3 cm and (b) 4 cm×4 cm. (c) Actual infrared (IR) thermal images and (d) corresponding COMSOL simulated temperature distribution of the 3 cm×3 cm and 4 cm×4 cm evaporators after 12 h of operation. (e) Time-dependent evaporation rates and (f) the corresponding salt collection rate for evaporators of varying sizes over 12 h. (g) Schematic illustration of the "Evaporation Dead Zone" mechanism over a large-area evaporator, where non-uniform lateral vapor transport leads to severe humidity accumulation in the center, thereby thermodynamically suppressing the local evaporation rate.

To address the scale-dependent transport limitations and evaluate the potential risk of central salt accumulation, we fabricated scaled-up monolithic evaporators with continuous areas of 3 cm×3 cm and 4 cm×4 cm. The devices were tested in highly concentrated 10 wt% NaCl brine for 12 h. As presented in **Figure S41a, b**, optical observations and corresponding COMSOL multiphysics simulations reveal that no central salt accumulation occurred in these larger devices. Salt crystallization was still successfully confined to the edges. However, a minor, localized salt accumulation was observed at the extreme distal end (furthest from the water supply) of the 4 cm×

4 cm PVIL hydrogel evaporator. This slight distal accumulation objectively indicates that the 4 cm× 4 cm dimension is approaching the threshold of the system's physical lateral transport limits. Furthermore, while catastrophic salt fouling was successfully averted, mass transport is not the only scaling constraint; we observed a distinct scale-dependent performance degradation driven by thermal imbalances. As shown in **Fig. S41e, f** the overall evaporation rate and salt collection efficiency decreased as the device area increased. Based on our simulation and experimental thermal profiles (**Fig. S41c, d**), the central regions of the scaled-up evaporators exhibited noticeably higher temperatures than the edges. This thermal behavior is a classic signature of the "Humidity Dead Zone" **(Fig. S41g)**. As the continuous evaporation area expands, the water vapor generated in the central region cannot diffuse laterally fast enough, leading to localized vapor accumulation. According to thermodynamic principles, this high-humidity boundary layer severely suppresses the local phase-change process. Consequently, less heat is consumed as latent heat of evaporation in the center, causing the observed rise in sensible heat.

Therefore, we conclude that the primary bottleneck limiting the monolithic scale-up of solar evaporators is not strictly the lateral ion transport, but rather the aerodynamic vapor transport[2, 3]. This physically validates that blindly increasing the monolithic material size is suboptimal. To fundamentally decouple the evaporation efficiency from the device scale, an optimized modular or array-based design is imperative. By partitioning the system, we can maintain a high edge-to-area ratio for salt removal while simultaneously providing critical ventilation channels to disrupt the humidity dead zone, thereby ensuring scalable, high-efficiency water-salt-electricity co-generation.

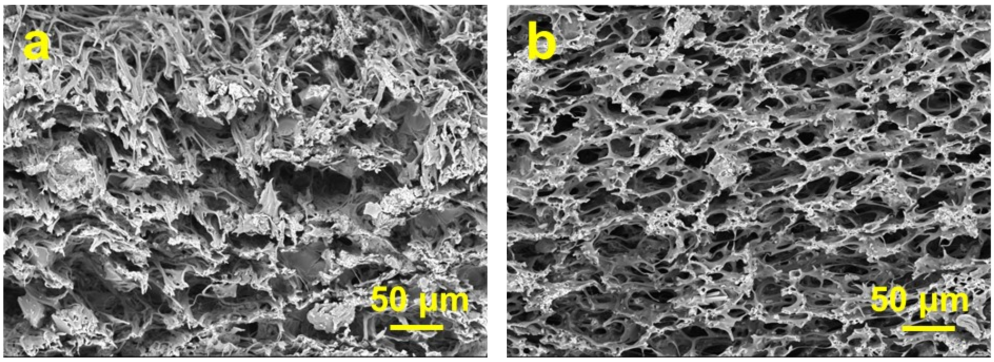

Fig. S42. (a) SEM image of the PVIL hydrogel after 8 h of continuous illumination (1 sun), showing partial pore blockage by salt accumulation. (b) SEM image of the PVIL hydrogel after a subsequent 16 h resting period in the dark (without illumination), showing that the pores are restored due to salt redissolution.

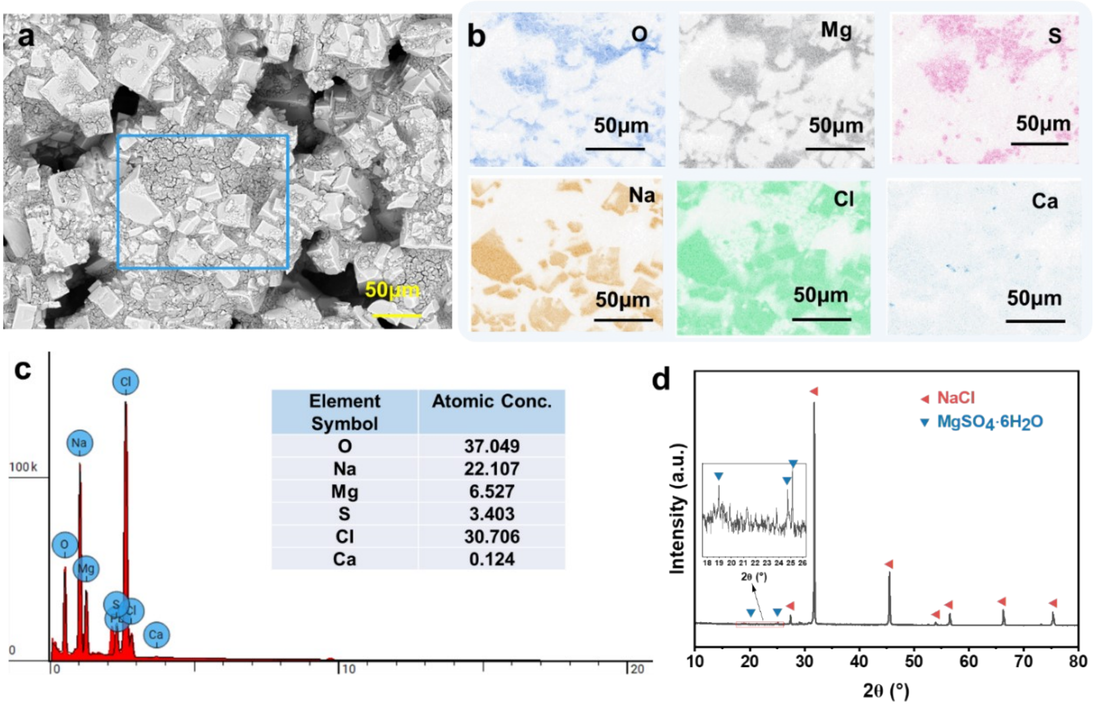

Element Symbol	Atomic Conc.
O	37.049
Na	22.107
Mg	6.527
S	3.403
Cl	30.706
Ca	0.124

Fig S43. (a) SEM image of the edge-crystallized salts. (b) Corresponding EDS elemental mapping (O, Mg, S, Na, Cl, and Ca) of the selected region in (a). (c) EDS spectrum and the quantified atomic concentrations of the constituent elements in the harvested salts. (d) X-ray diffraction pattern of the collected solid salts from the lateral edges.

Fig. S43 presents the morphological and compositional characterization of the salts harvested from the evaporator edges during the concentrated seawater test. The SEM image (**Fig. S43a**) reveals the crystal morphology of the edge-precipitated salts. Corresponding EDS elemental mapping (**Fig. S43b**) shows the spatial distribution of O, Mg, S, Na, Cl, and Ca within the selected region, indicating the coexistence of multiple ions. The EDS spectrum and quantified atomic concentrations (**Fig. S43c**) further confirm the elemental composition of the harvested salts. Finally, the X-ray diffraction pattern (**Fig. S43d**) identifies the crystalline phases, including NaCl and $MgSO_4·6H_2O$, corroborating the formation of mixed salts under multicomponent brine conditions [4].

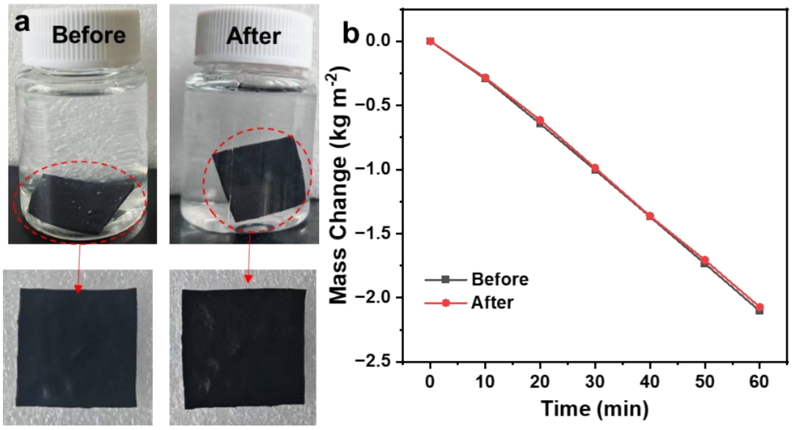

Fig. S44. (a) Optical images, (b) evaporation rates of PVIL hydrogel before and after 2 days of ultrasound.

Fig. S44a displays optical images of PVIL in pure water before and after two days of ultrasonication, showing no damage. **Fig. S44b** illustrates the evaporation rate of PVIL in pure water before and after ultrasonication, revealing no decrease whatsoever. These results underscore the PVIL hydrogels' durability, a critical requirement for long-term solar evaporation applications. The retained structural and functional stability after ultrasonication further validates the hydrogels' suitability for scalable, real-world brine treatment systems.

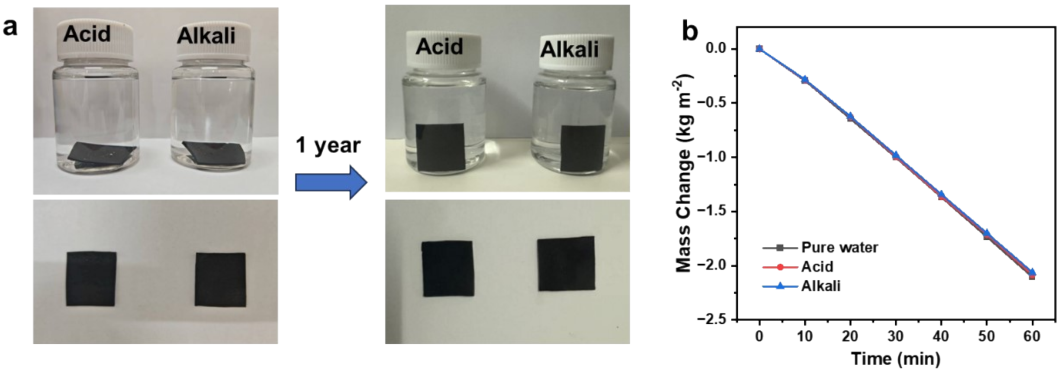

Fig. S45. (a) Optical images of PVIL hydrogel before and after 1 year of immersion in solutions at pH=1 and pH=14. (b) Pure water evaporation rate of PVIL hydrogel after 1 year of immersion in acidic and alkaline solutions.

Fig. S45 demonstrates the exceptional long-term stability of PVIL hydrogels for harsh-environment applications: after 1 year of immersion in pH=1 (acidic) and pH=14 (alkaline) solutions, the hydrogels retained their structural integrity (no visible damage, **Fig. S45a**), enabled by abundant covalent bonds and multiple non-covalent interactions, and evaporation performance unchanged rates in pure water **(Fig. S45b)**. This robust resistance to chemical corrosion and mechanical degradation, rare in hydrogel, based systems, validates their suitability for sustainable, long-term industrial brine treatment, a key enabler for scalable ZLD technologies.

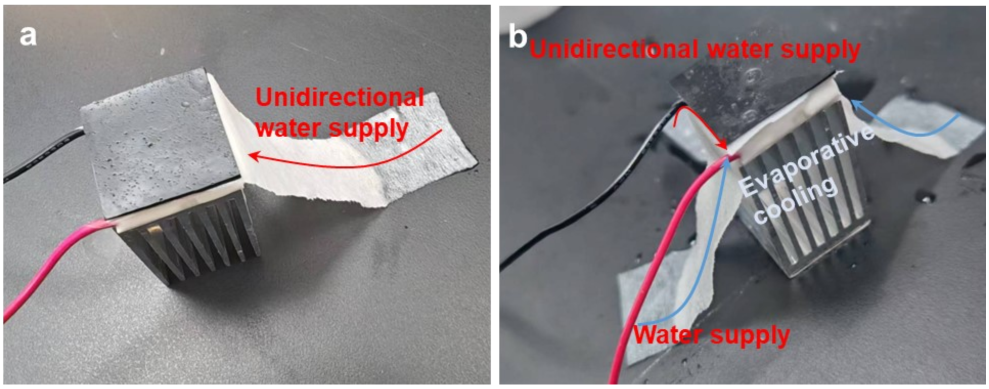

Fig. S46. Schematic diagram of the PVIL-TEG device. (a) The TEG base connects directly to the heat sink. (b) A bidirectional water supply bibulous paper is positioned beneath the TEG base.

Fig. S46 demonstrates a latent heat-assisted cooling to enhance TEG performance. Unlike conventional heat-sink cooling, which suffers from efficiency decay due to interfacial thermal resistance, this approach places a wettable paper between the TEG cold side **(Fig. S46a)**. Capillary action draws liquid from a bulk water for evaporative cooling, enabling directly lowers the cold-side temperature **(Fig. S46b)**.

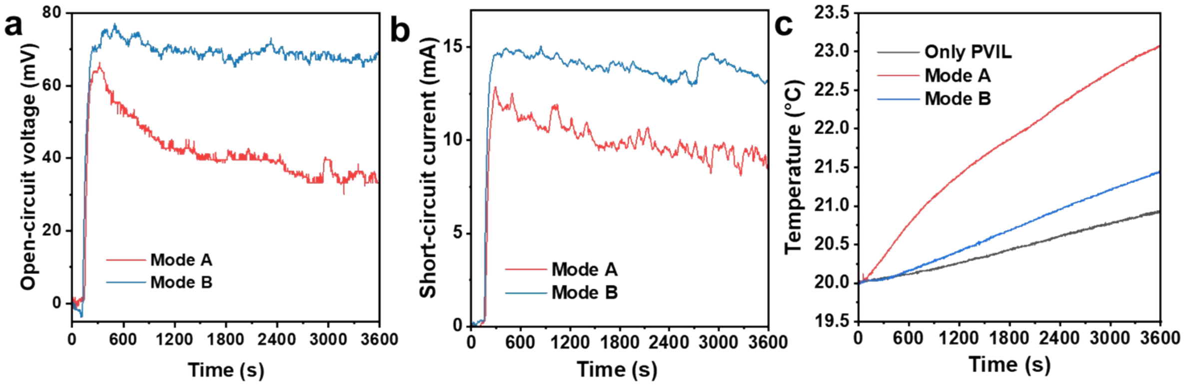

Fig. S47. (a) Time-dependent open-circuit voltage (V_{oc}) profiles for Mode A and Mode B under 1 sun irradiation (1 kW m^{-2}) over 3600 s. (b) Time-dependent short-circuit current (I_{sc}) profiles for Mode A and Mode B under 1 sun irradiation (1 kW m^{-2}) over 3600 s. (c) Real-time temperature evolution of the bulk water reservoir for mode A, Mode B, and only PVIL evaporator during operation.

Fig. 47a, b presents the V_{oc} and I_{sc} stability under continuous 1-sun illumination for 1 h. Mode B demonstrates superior stability, maintaining a high and steady voltage and current output with negligible decay after the initial rise. Conversely, Mode A exhibits a significant voltage drop shortly after reaching its peak. This instability in Mode A is attributed to the rapid accumulation of heat at the cold junction. The superior heat dissipation of Mode B is further confirmed by the temperature rise of the bottom 15 g water **(Fig. 47c)**. In the PVIL-only system (without TEG), the water temperature increases by only 0.9 °C over 3600 s. After integrating the TEG, Mode A shows a continuous and significant temperature rise of 3 °C, indicating that a large amount of heat is conducted directly into the bulk water through the radiator. However, this heat is not utilized for evaporation or electricity generation, leading to thermal pollution and additional parasitic heat loss. In contrast, Mode B exhibits a much slower temperature increase of only 1.5 °C over the same period, confirming that the bibulous paper consumes thermal energy through phase-change evaporation rather than transferring it to the water tank.

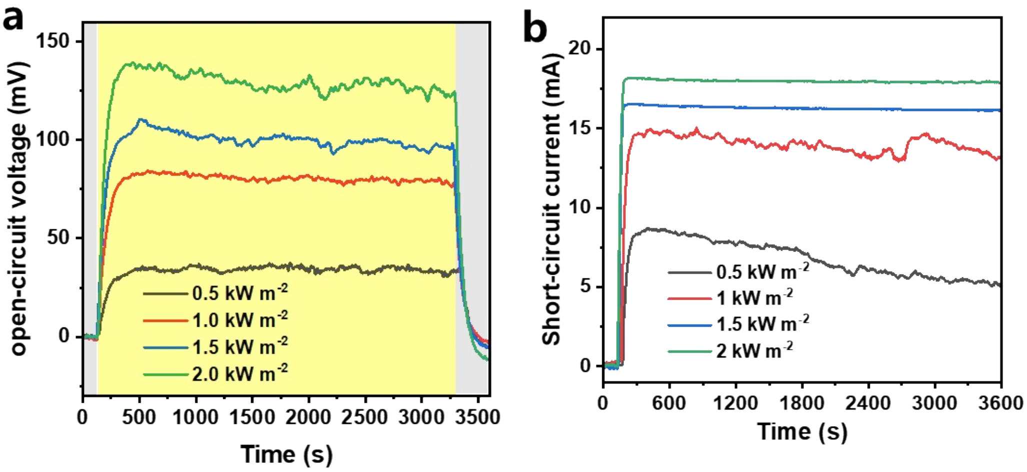

Fig. S48. (a) V_{oc} of PVIL-TEG Mode B system at different light intensity. (b) I_{sc} of PVIL-TEG Mode B system at different light intensity.

Fig. S48 shows the short-circuit current of PVIL-TEG under varying light intensities, with the V_{oc} and I_{sc} gradually increasing as light intensity rises.

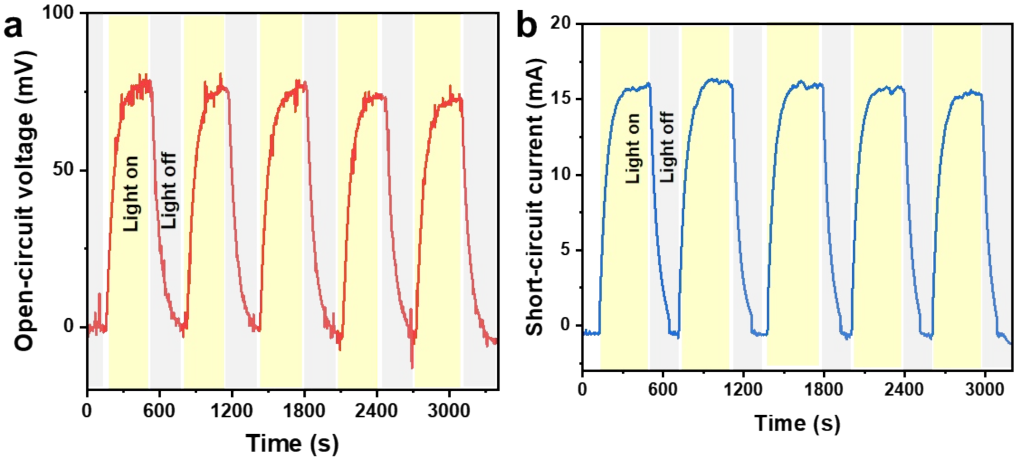

Fig. S49. (a) V_{oc} and (b) I_{sc} cycle stability of PVIL-TEG under light on and light off conditions.

Fig. S49 demonstrates the repeatable performance of the PVIL-TEG under 1-sun illumination. The open-circuit voltage rapidly rises to ~75 mV when "Light on" and drops to near 0 mV upon "Light off," with negligible degradation over 5 consecutive cycles. The short-circuit current exhibits a consistent response, reaching ~16 mA during illumination and returning to baseline in the dark, maintaining stability for 3200 s.

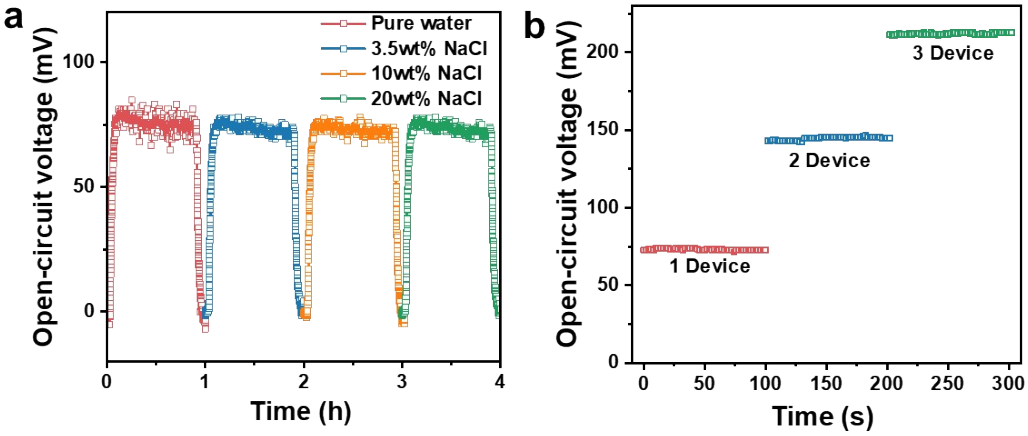

Fig. S50. (a) Durability of the hybrid device using pure water and different concentrations of NaCl (solar intensity: 1 kWm^{-2}). (b) The V_{oc} generated by connecting different numbers of TEGs in series.

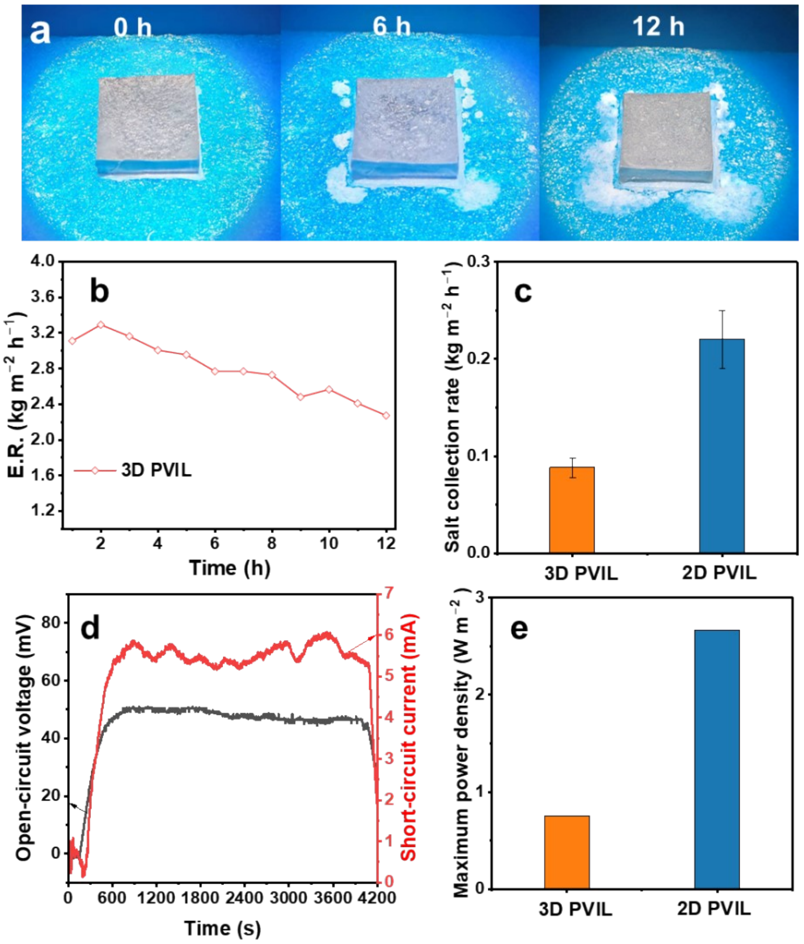

Fig. S51. (a) Optical images of the 3D PVIL evaporator at 0, 6, and 12 h. (b) Evaporation rates of 3D PVIL evaporators in 10 wt% NaCl. (c) Salt collection yields of 3D and 2D PVIL hydrogel evaporator. (d) V_{oc} and I_{sc} of 3D PVIL hydrogel evaporator integrated TEG. (e) Maximum power density of 3D and 2D PVIL hydrogel evaporator.

To evaluate the effect of evaporator geometry on overall performance, we compared the 2D (height: 1mm) and 3D (height: 1cm) PVIL hydrogel evaporators under identical conditions (10 wt% NaCl, 1 sun, 12 h). As shown in **Fig. S51a**, the 3D evaporator exhibited salt accumulation primarily inside the matrix rather than at the edges, due to the extended ion transport pathways. Consequently, its evaporation rate gradually declined over the 12 h period (**Fig. S51b**). The salt collection yield of the 3D evaporator was substantially lower than that of the 2D counterpart (**Fig. S51c**). Moreover, the increased thickness of the 3D device led to higher thermal resistance and a reduced temperature gradient across the thermoelectric module, resulting in lower V_{oc}, I_{sc} (**Fig. S51d**) and maximum power density (**Fig. S51e**) compared to the 2D system. These results demonstrate that while a 3D architecture may offer a larger evaporation surface, the trade-offs in ion transport and thermal management compromise long-term stability and co-generation efficiency, validating the advantage of the 2D design for sustainable brine treatment.

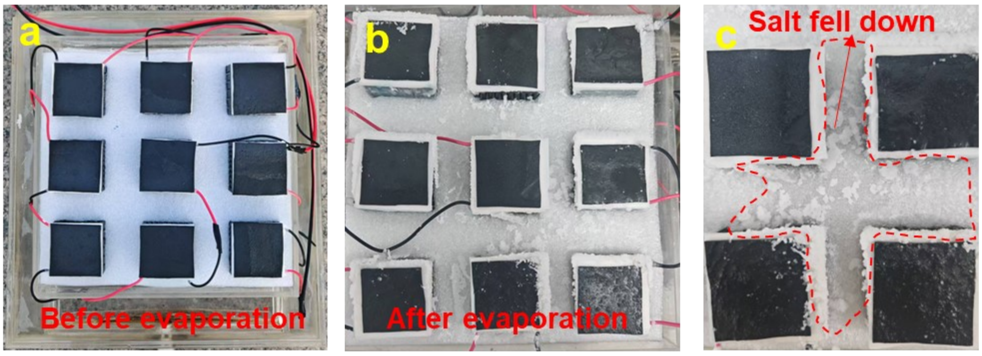

Fig. S52. Optical images of the PVIL-TEG system (a) before and (b) after evaporation under natural light conditions. (c) Salt crystallizing and shedding at the edges.

Fig. S52 (a, b) displays images of the PVIL hydrogel evaporator before and after outdoor evaporation experiments. The small amount of accumulated salt on surfaces could be easily removed via simple scraping, owing to the loose, non-adherent nature of the salt crystals. **Fig. S52c** illustrates that during operation, salt migrated to the periphery of the evaporator and fell off spontaneously under gravity. This peripheral salt accumulation, rather than internal clogging, ensures unobstructed liquid transport and vapor diffusion within the evaporator. The gravity-driven detachment of peripheral salt further eliminates the need for active cleaning, reducing maintenance burden. The ability to easily scrape surface salt and the spontaneous detachment of peripheral salt minimize downtime, making the system highly suitable for sustainable ZLD applications.

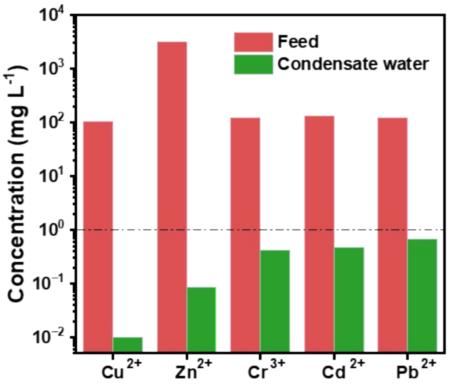

Fig. S53. Heavy metal concentrations before and after purification.

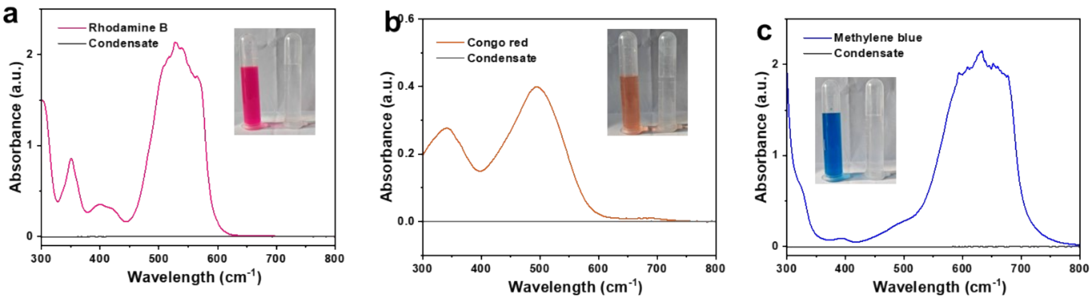

Fig. S54. (a) Rhodamine B, (b) Congo red, and (c) methylene blue content before and after purification.

Fig. S54 shows the UV-Vis absorption spectra of the feed and purified water for solutions containing RhB, Congo red, or methylene blue (50 mg L^{-1} each). The absence of characteristic absorption peaks in the condensate indicates exceptionally high dye rejection and decolorization efficiency.

Fig. S55. pH values of acidic and alkaline solutions before and after purification.

The PVIL evaporator demonstrates self-neutralizing purification functionality for both acidic and alkaline feed waters. As shown in **Fig. S55**, the condensate from extreme pH solutions (original pH = 1 and 14) was neutralized to pH 6-7, indicating its potential for treating industrial wastewaters with fluctuating pH levels.

Section 3. Supporting tables

Table S1. Salt compositions of simulated seawater and its concentrated brines.

Salt	1× (seawater)	2× concentrated	3× concentrated	4× concentrated
NaCl	24.14 g	48.28 g	72.42 g	96.56 g
Na_2SO_4	4.01 g	8.02 g	12.03 g	16.04 g
KCl	0.76 g	1.52 g	2.28 g	3.04 g
$CaCl_2\cdot$	1.50 g	3.00 g	4.50 g	6.00 g
$MgCl_2\cdot 6H_2O$	10.79 g	21.58 g	32.37 g	43.16 g
Total salt mass	41.20 g	82.40 g	123.60 g	164.80 g

Note: The above masses are for preparing 1 L of each solution. The total dissolved solids (TDS) of the simulated seawater are approximately 35 g L^{-1}, and the concentrated brines have TDS of approximately 70 g L^{-1} (2×), 105 g L^{-1} (3×), and 140 g L^{-1} (4×).

Table. S2. Comparison of salt collection performance between our PVIL hydrogel device and previous devices using evaporators.

Materials of evaporators	**Salt collection rate ($g\ m^{-2}\ h^{-1}$)**	**Operation time (h)**	**Ref**
Nylon 66/carbon black nanofiber film, Sol. RRL (2022)21	55 (3.5wt% NaCl) 124 (10wt% NaCl) 151 (15wt% NaCl)	9 (3.5 wt.%, 10wt%, 15 wt.% NaCl)	5
Printed air-laid paper, Desalination (2020)22	25 (3.5wt% NaCl)	12 (3.5wt% NaCl)	6
Functionalized polyacrylonitrile textile, Chem. Eng. J. (2021)23	20 (7.5wt% NaCl)	60 (7.5wt% NaCl)	7
MOFs-based nanorod arrays, Desalination (2022)24	47	120	8
Carbon nanotube-embedded filter paper discs, Energy Environ. Sci. (2019)	38	630	9
3D nitrocellulose membrane, Environ. Sci. Technol. (2023)25	97 (10wt% NaCl)	240 (10 wt% NaCl)	10
Nano/micro-structured titania layer on titanium mesh, Nat. Commun. (2024)26	7.5 (3.5 wt% NaCl) 11.6 (7 wt% NaCl) 33.2 (12 wt% NaCl)	96 (3.5 wt% NaCl)	11
Polyacrylamide-modified carbonized bamboo fiber, Energy Environ. Sci. (2024)	40 (3.5 wt% NaCl)	1800 (3.5 wt% NaCl)	12
This work	240 (10 wt% NaCl)	3648 (10 wt% NaCl)	

Table S3. Simplified energy balance analysis of the PVIL and PVIL–TEG systems under 1 sun irradiation

System	Q_{evap} (W m^{-2})	Q_{elec} (W m^{-2})	Q_{cond} (W m^{-2})	Q_{other} (W m^{-2})
PVIL only	949.1	0	39.4	11.5
Mode A	677.9	1.01	131.3	189.7
Mode B	885.8	2.55	61.3	50.3

To clarify the practical contribution of thermoelectric integration, a simplified energy-balance analysis was conducted for three configurations under 1 sun irradiation: the PVIL-only evaporator (without TEG), the PVIL–TEG system with conventional heat-sink cooling (Mode A), and the PVIL–TEG system with latent heat-assisted evaporative cooling (Mode B). The incident solar power was partitioned into four terms: evaporation-associated power (q_{evap}), electrical output (q_{elec}), downward conductive heat transfer into the underlying water reservoir (q_{cond}), and the remaining unaccounted losses (q_{other}).

Illuminated area:

$A = 2\ cm \times 2cm\ = 4.0 \times 10^{-4}\ \mathrm{m}^2$

Irradiation intensity: $q_{in} = 1000\ \mathrm{W\ m^{-2}}$

Irradiation time: $t = 1\ \mathrm{h} = 3600\ \mathrm{s}$

Evaporation enthalpy of water in PVIL hydrogel: $h_{evap} = 1627\ \mathrm{J\ g^{-1}}$

Mass of underlying water reservoir: $m = 15\ \mathrm{g}$

Specific heat capacity of water: $c = 4.2\ \mathrm{J\ g^{-1}K^{-1}}$

1. Evaporation-associated power, q_{evap}

The evaporation-associated power was calculated from the measured evaporation rate:

$$q_{evap} = \frac{E \times 1000 \times h_{evap}}{3600}$$

where:

$E$is the evaporation rate in $\mathrm{kg\ m^{-2}h^{-1}}$

(a) PVIL only

$$q_{evap} = \frac{2.10 \times 1000 \times 1627}{3600} = 949.1\ \mathrm{W\ m^{-2}}$$

(b) Mode A

$$q_{evap} = \frac{1.50 \times 1000 \times 1627}{3600} = 677.9\ \mathrm{W\ m^{-2}}$$

(c) Mode B

$$q_{evap} = \frac{1.96 \times 1000 \times 1627}{3600} = 885.8\ \mathrm{W\ m^{-2}}$$

2. Electrical power density, q_{elec}

The electrical contribution was taken directly from the measured power density of the TEG.

(a) PVIL only

$q_{elec} = 0\ \mathrm{W\ m^{-2}}$

(b) Mode A

$q_{elec} = 1.01\ \mathrm{W\ m^{-2}}$

(c) Mode B

$q_{elec} = 2.55\ \mathrm{W\ m^{-2}}$

3. Downward conductive heat transfer into the underlying water, q_{cond}

The heat accumulated in the underlying water reservoir during 1 h was calculated as:

$Q_{cond} = cm\Delta T$

$$q_{cond} = \frac{Q_{cond}}{At}$$

Where Q is the heat flux, C is the specific heat capacity of water (4.2 kJ °C^{-1} kg^{-1}), m is the weight of bulk water used in the experiment (15 g), ΔT is the temperature change of the bulk water after evaporation for 1 h.

The downward conductive heat loss under the three modes is derived from the temperature rise curves shown in Fig. 47c.

Since $At = 4.0 \times 10^{-4} \times 3600 = 1.44\ \mathrm{m^2 \cdot s}$

(a) PVIL only

$Q_{cond} = 15 \times 4.2 \times 0.9 = 56.7\ \mathrm{J}$

$$q_{cond} = \frac{56.7}{1.44} = 39.4\ \mathrm{W\ m^{-2}}$$

(b) Mode A:

$Q_{cond} = 15 \times 4.2 \times 3.0 = 189.0\ \mathrm{J}$

$$q_{cond} = \frac{189.0}{1.44} = 131.3\ \mathrm{W\ m^{-2}}$$

(c) Mode B

$Q_{cond} = 15 \times 4.2 \times 1.4 = 88.2\ \mathrm{J}$

$$q_{cond} = \frac{88.2}{1.44} = 61.3\ \mathrm{W\ m^{-2}}$$

4. Other unaccounted losses, q_{other}

The remaining power density (such as surface reflection, thermal radiation to the environment, convective heat loss to the ambient air) was estimated by subtracting the above three contributions from the incident solar input:

$q_{other} = q_{in} - q_{evap} - q_{elec} - q_{cond}$

where:

$q_{in} = 1000\ \mathrm{W\ m^{-2}}$

(a) PVIL only

$q_{other} = 1000 - 949.1 - 0 - 39.4 = 11.5\ \mathrm{W\ m^{-2}}$

(b) Mode A

$q_{other} = 1000 - 677.9 - 1.01 - 131.3 = 189.7$ W m^{-2}

(c) Mode B

$q_{other} = 1000 - 885.8 - 2.55 - 61.3 = 50.3$ W m^{-2}

Because the radiator itself dissipates heat directly to the surrounding air (Mode A), the remaining energy loss is higher than that in the evaporative cooling mode (Mode B) and in the system without a TEG (PVIL-only).

Table S4. A comparison of the photothermal evaporation performance and thermoelectric power generation between recently reported materials under 1 sun irradiation.

Materials of evaporators	**E.R. (kg m^{-2} h^{-1})**	**Power (W m^{-2})**	**Ref**
CuS-rGO pyramidal structure	2.29	1.32	[13]
Sulfide/Nickel Foam Based Solar Evaporator	1.29	0.18	[14]
SandwichStructured All-DayRound Solar Evaporator (2022)24	2.67	0.42	[15]
Carbon Nanostruct ure Absorber	1.37	1.33	[16]
Porous CMF/Cu@ CuS foam	1.85	0.69	[17]
MnO/C hybrid nanoparticle	2.38	0.77	[18]
Nanoclay Hybridized Graphene Aerogels	2.13	1.57	[19]
Zwitterionic fibrous membrane	2.64	1.50	[20]
This work	1.96	2.55	

Techno-Economic Analysis: Cost Calculation and Economic Viability as a ZLD Technology

This section presents a techno-economic analysis of the proposed gel-based material for achieving ZLD. The evaluation focuses solely on the process of brine concentration and salt crystallization, excluding power generation, to isolate the economic viability of the core ZLD function. The analysis scales up the laboratory for a 2 cm × 2 cm sample to a 1 m^2 system, utilizing industrial wholesale prices for input materials and market prices for the recovered salt. The cost of bibulous paper, used for supplying water to the material, is included for comprehensiveness.

Table S5. Material formulation and cost for the 1 m^2 sample.

Component	Mass for 1 m^2 (kg)	Active Mass (kg)	Unit Price (USD/kg)	Cost (USD)
PVA	0.900	0.090	1.500	0.1350
H_2SO_4	0.350	0.175	0.030	0.0052
HCHO	0.0750	0.0750	0.90	0.067
VEIMBr	0.1500	0.1470	25.00	3.75
MBA	0.0150	0.0150	5.00	0.075
Graphite Powder (GP)	0.0150	0.0150	0.02	0.0003
Bibulous Paper	0.040	0.0400	0.01	0.0004
Process Water		1.012	0.0007	0.0007
Total Cost for 1 m^2				~3.9 USD

Revenue from Recovered Salt at Different Market Prices

The system processes 8.2 tons of brine over a 152-day operational cycle per square meter, producing 0.86 tons (860 kg) of NaCl as a marketable salt product.

The revenue from recovered salt (R_{salt}) and payback period are highly sensitive to the market value of the salt. We analyze two price scenarios:

Scenario A: High-Purity/Reagent-Grade price (10 USD/kg)

Revenue: $R_{salt} = 860 \text{ kg} \times 10 \text{ USD/kg} = 8600 \text{ USD}$

Net Profit per cycle (P_{net}): $P_{net} = R_{salt} - C_{material} = 8600 - 3.9 \approx 8596.1 \text{ USD}$

Payback Period (PP):

$$PP = \frac{C_{material}}{P_{net}} \times 152 \text{ days} \approx \frac{3.9}{8596.1} \times 152 \approx 0.069 \text{ days (1.6 h)}$$

Scenario B: Conservative Industrial-Grade Salt Price (0.14 USD/kg, equivalent to 140 USD/ton)

Revenue: $R_{salt} = 860 \text{ kg} \times 0.14 \text{ USD/kg} = 120.4 \text{ USD}$

Net Profit per cycle (P_{net}): $P_{net} = R_{salt} - C_{material} = 120.4 - 3.9 = 116.5 \text{ USD}$

$$PP = \frac{C_{material}}{P_{net}} \times 152 \text{ days} \approx \frac{3.9}{116.5} \times 152 \approx 5 \text{ days}$$

Conclusion:
The techno-economic analysis confirms the high economic potential of salt recovery. Even at a conservative industrial price for edible salt (0.14 USD/kg), the revenue from salt alone enables a remarkably short payback period of approximately 5 days for the material investment. If the produced salt can command a higher market value, such as that of high-purity or specialty salts (10 USD/kg), the payback period becomes negligible (less than 2 h), underscoring the transformative economic viability of this ZLD approach.

Economic Analysis with Condensation Cover Cost (Water Revenue Only)

1. Cost Assumptions and Parameters

Material Cost (PVIL): $C_{material}$ = 3.9 USD m^{-2}

Condensation Cover Cost: A transparent acrylic cover (dimensions: 1 m × 1 m × 0.25 m, five-sided) is required. The industrial wholesale price of 7.5 USD m^{-2} for 3-mm-thick acrylic sheets, the total cost is:

$C_{condenser}$ =15 USD

Total Initial Investment: $C_{total} = C_{material} + C_{condenser}$ = 3.9 + 15 = 18.9 USD m^{-2}

Water Production Rate: W_{daily} = 6.3 kg m^{-2} day^{-1} = 6.3 L m^{-2} day^{-1} (assuming water density of 1 kg L^{-1})

Water Price Scenarios:

Scenario A (Bottled Water): $P_{bottled}$= 0.43 USD L^{-1}

Scenario B (Tap Water): P_{Tap} = 7 × 10^{-4} USD L^{-1} = 0.0007 USD L^{-1}

Payback Period Calculation Based on Daily Water Revenue

The PP is calculated as the total initial investment divided by the daily net revenue from water sales: PP = C_{total} / (W_{daily} × P_{water}).

Scenario A (Bottled Water Price):

Daily Revenue: R_{daily} = 6.3 L day^{-1} × 0.43 USD L^{-1} = 2.709 USD day^{-1}

Payback Period: PP_A = 18.9 USD / 2.709 USD day^{-1} ≈ 7.00 day

Scenario B (Tap Water Price):

Daily Revenue: R_{daily} = 6.3 L day^{-1} × 0.0007 USD L^{-1} ≈ 0.00441 USD day^{-1}

PP_B = 18.9 USD / 0.00441 USD day^{-1} ≈ 4302 days ≈ 11.8 years

Conclusion:

When incorporating the cost of a condensation cover, the total initial investment for the PVIL-based system is estimated to be 18.97 USD m^{-2}. Considering water production revenue alone:

If the produced freshwater is sold at a bottled water price (0.43 USD L^{-1}), the exceptionally high revenue stream yields a payback period of approximately 7 days.

If the water is valued at a municipal tap water price (0.0007 USD L^{-1}), the payback period extends to approximately 11.8 years.

However, the primary deployment scenarios for the PVIL hydrogel are off-grid, resource-scarce environments—such as remote islands, arid coastlines, and disaster-stricken areas—where centralized water infrastructure is either nonexistent or prohibitively expensive to install. In these contexts, the 'competitor' is not cheap tap water, but rather expensive transported bottled water. Furthermore, the freshwater produced by the PVIL evaporator is high-purity distillate with significantly lower ion concentrations than municipal standards (as verified in Fig. 6d), rendering it superior for direct drinking or high-value industrial use. Therefore, considering its portability, independence from infrastructure, and superior water quality, the PVIL system offers a decentralized water security solution that complements, rather than competes with, centralized municipal grids.

Reference:

1. A. F. Eskafi, C. De Finnda, C. A. Garcia and B. Mi, *Environ. Sci. Technol.*, 2025, **59**, 892-901..
2. X. Li, J. Li, L. Zou, M. Chen, H. Wang, L. Yang, R. Yang, H. Zhang and Y. Zhou, Adv. Funct. Mater., 2025, 35,2504502.
3. T. Gao, Y. Wang, X. Wu, P. Wu, X. Yang, Q. Li, Z. Zhang, D. Zhang, G. Owens and H. Xu, Sci. Bull., 2022, 67, 1572-1580.
4. Y. Liu, Y. Lian, J. Chen, A. Baqais, C. Wang, J. Chen, C. Lin, C. Wang, Z. He, B. Liu, Y. Jiang, D. M. Al Shamsi, A. Al Raeesi, M. Sherif, J. Cao, W. Wang and P. Wang, Sci. Adv., 2026, 12, eaeb2604.
5. J. Mao, J.-J. Li, A.-Q. Xie, Y. Liang, Y. Yang, L. Zhu and S. Chen, *Sol. RRL*, 2022, **6**, 2200330.
6. J. Xu, Z. Wang, C. Chang, B. Fu, P. Tao, C. Song, W. Shang and T. Deng, *Desalination*, 2020, **484**, 114423.
7. H. Peng, D. Wang and S. Fu, *Chem. Eng. J.*, 2021, **426**, 131818.
8. X. Ma, X. Wan, Z. Fang, Z. Li, X. Wang, Y. Hu, M. Dong, Z. Ye and X. Peng, *Desalination*, 2021, **522**, 115399.
9. Y. Xia, Q. Hou, H. Jubaer, Y. Li, Y. Kang, S. Yuan, H. Liu, M. W. Woo, L. Zhang, L. Gao, H. Wang and X. Zhang, *Energy Environ. Sci.*, 2019, **12**, 1840-1847.
10. Z. Yang, D. Li, K. Yang, L. Chen, J. Wang, X. Zhu and B. Chen, *Environ. Sci. Technol.*, 2023, **57**, 13047-13055.
11. M. A. Abdelsalam, M. Sajjad, A. Raza, F. AlMarzooqi and T. Zhang, *Nat. Commun.*, 2024, **15**, 847.
12. Y. Wu, C. Ma, K. Zhu, L. Jin, L. Song, L. Li, Y. Lu, Y. Zheng, Y. Zhang, X. Zheng, S. Wu, Y. Pang, Z. Shen, S. C. Tan and H. Chen, *Energy Environ. Sci.*, 2024, **17**, 9303-9312.
13. L. Zeng, D. Deng, L. Zhu, Z. Zhang, X. Gu, H. Wang and Y. Jiang, *Nano Energy*, 2024, **125**, 109531.
14. H. Jiang, L. Ai, M. Chen and J. Jiang, *ACS Sustainable Chem. Eng.*, 2020, **8**, 10833-10841.
15. R. Niu, J. Ren, J. J. Koh, L. Chen, J. Gong, J. Qu, X. Xu, J. Azadmanjiri and J. Min, *Adv. Energy Mater.*, 2023, **13**, 2302451.
16. P. Cheng and D. Wang, *ACS Appl. Mater. Interfaces*, 2023, **15**, 8761-8769.
17. H. Wang, Y. Song, T. Li, Z. Xiuwen, G. Shanmin and L. Jun, *J. Mater. Chem. A*, 2022, **11**, 419-433.
18. Z. Fan, J. Ren, H. Bai, P. He, L. Hao, N. Liu, B. Chen, R. Niu and J. Gong, *Chem. Eng. J.*, 2023, **451**, 138534.
19. Y. Tang, X. Zhao, Y. Li, Z. Yang, X. Zuo, A. Tang and H. Yang, *Adv. Funct. Mater.*, 2024, 34, 2408693.
20. Y. Wang, F. Chen, Q. Chen, W. Liu, Q. Huang, X. Hou, S. Li, C. Cheng, X. Xie, N. Meng and Y. Liao, *Nat. Commun.*, 2025, **16**, 6373.